ACS OMEGA

Open Access

http://pubs.acs.org/journal/acsodf

Review

Diamond Color Center Based Quantum Metrology in Industries for Energy Applications

Tanmoy Basu,* Anupam Patra, Midhun Murali, Mahesh Saini, Amit Banerjee, and Tapobrata Som

Cite This: *ACS Omega* 2025, 10, 2372−2392

Read Online

ACCESS | Metrics & More | Article Recommendations

ABSTRACT: Atomic scale defects in diamond are emerging as next-generation quantum sensors. One such defect is the nitrogen vacancy (NV) center which possesses artificial atom-like properties making it a strong contender for a room temperature solid state qubit. These spin defects are optically addressable by studying their optically detected magnetic resonance spectra (ODMR). The spin states can be initialized, controlled, and read out by a shining laser. The photoluminescence spectra contain information on the external magnetic field, electric field, temperature, etc. Thus, this type of multimodal sensor is exigent in various fields of research viz. chemistry, materials science, biology, and fundamental physics. In today's world where energy-related products are booming, deployment of quantum sensors can expedite the development. Based on existing works, this paper makes an attempt to identify the applications of color centers in diamond for energy sectors. We have highlighted the efficacy of quantum diamond sensors in the oil and gas industry, battery research, and photovoltaics. In addition, a summary of the structural and quantum properties of defects in diamond, synthesis of diamond, protocols for optical detection of spin states, different types of color centers, etc., is presented.

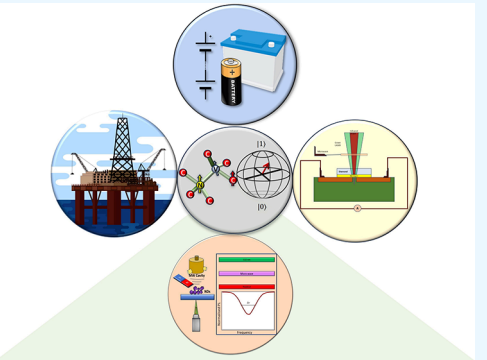

1. INTRODUCTION

If we look toward the status of present quantum technology related research works, quantum sensing has surfaced as a domain which has the potential for harnessing the power of the quantum world in real-life applications in the near term. These sensors can perform measurements of certain physical quantities by utilizing quantum coherence, entanglement, and superposition to accomplish sensitivities beyond a classical limit.[1] Various platforms exist for quantum sensing including spin qubits,[2] cold atoms,[3] trapped ions,[4] superconducting qubits,[5] photons,[6] and certain materials with two-level system-like characteristics.[7] Quantum sensors can be used to detect a magnetic field,[8] electric field,[9] temperature,[10] gravitational field,[11] and other quantities with high precision.[12]

However, many of these quantum sensors need cryogenic cooling or vacuum-based operation. In addition, most of them are not immune to work under harsh conditions. An alternative emerging competitor is solid state spin qubits. In particular, nitrogen vacancy (NV) centers in a diamond can be used as a spin qubit that is capable of room temperature operation and can be easily formed with a diamond lattice.[13] In addition, they have relatively long coherence times even at room temperature which is also important for quantum computing application.[14] As a matter of fact, diamonds containing atomic scale defects have shown great potential by exhibiting multimodal sensing properties by detecting a magnetic field,[15] electric field,[16] temperature,[17] pressure,[18] pH,[19] thermal conductivity,[20] etc. The atomic scale defects in diamond can generate single photon emission and are known as "color centers". It may be pointed out that various defects can be incorporated in diamond, e.g. nitrogen,[21,22] silicon,[23] tin (SnV),[24] germanium (GeV),[25] etc. The main advantage of these solid-state spin qubits is that their photoluminescence spectra can be monitored experimentally to obtain different measurable physical quantities.

In this paper, we review the progress of color centers in diamond-based quantum sensors mainly from the perspective of energy related applications. We have identified three important areas viz. oil and gas industry, battery research, and photovoltaics, where these quantum diamond sensors are being used or have potential to be utilized in the near future. In passing, we have also discussed some fundamental properties of defects in diamond and how they can be induced into a diamond lattice. In addition, we have briefly described some of the emerging synthesis processes of making nanocrystalline diamond. Various detection protocols in context of diamond

Received: May 9, 2024
Revised: October 3, 2024
Accepted: October 18, 2024
Published: January 13, 2025

quantum sensing (with nitrogen vacancy centers) have been pointed out. It may be noted that this field of research is comparatively new and still evolving toward getting matured. Therefore, we have also highlighted relevant proposals that can be commercialized in later stages with the discovery of suitable fabrication methodology. However, the prospect of quantum diamond sensors for energy applications is difficult to find.

The extracted data from quantum diamond sensor can further be utilized for improving the efficiency of a solar cell, discovering fossil fuel-based reservoirs, or designing robust battery monitoring systems for electric vehicles.

2. CRYSTALLOGRAPHIC DEFECT CENTERS IN DIAMOND

The diamond crystal structure consists of two interpenetrating face-centered cubic (fcc) Bravais lattices, displaced along the body diagonal of the cubic cell by one-quarter of the diagonal's length. Each lattice point in the fcc Bravais lattice contains two identical atoms, separated by one-quarter of the cube's body diagonal.[26] The fundamental unit of the structure is a tetrahedron, where a carbon atom is at the center, and its four nearest neighbors are at the corners (or vice versa). Each atom forms four bonds with its nearest neighbors. The diamond's NV (Nitrogen-Vacancy) center is a heteromolecular fluorescent lattice defect. It forms when a nitrogen atom is substituted into the diamond lattice, alongside a neighboring carbon vacancy.[27−29] It possesses a bandgap of 5.47 eV, allowing transparency across the ultraviolet to infrared spectrum. Due to this wide bandgap, diamonds serve as effective electrical insulators. Moreover, their high mechanical strength can be attributed to a Young's Modulus of 1054 GPa.[30,31] Diamond's high thermal conductivity, biocompatibility, and chemical inertness provide significant benefits for accommodating impurity atoms of other materials, resulting in the development of diverse physical properties.[30]

Common imperfections in diamonds can arise from substitutional or interstitial impurities, which may occur naturally or be introduced artificially.[32] These point defects are primarily categorized into two types: one featuring significant nitrogen impurity (Type I) and the other with nearly 1 ppm of nitrogen concentration (Type II). Type I is further divided into Type Ia (with nitrogen concentrations ranging from 500 to 3000 ppm) and Type Ib (with nitrogen concentrations below 300 ppm). Type II is subdivided into Type IIa and Type IIb based on boron impurity's absence or presence, respectively.[30,33−36] NV centers are structural defects wherein a carbon atom adjacent to a vacancy (referred to as a "missing atom") in a diamond crystal or thin film is substituted by a nitrogen atom. This substitution gives rise to a mobile electron and a vacancy close by (Figure 1).

Although NV centers are found in natural diamond, based on our application, we can introduce a single or ensemble of NV centers in diamond by different engineering techniques. This flexibility also applies to lab-grown nanodiamonds. All this versatility of diamond structure, diamond with single NV center, ensemble of NV centers in nano diamonds and bulk diamonds, significantly impacts the overall sensitivity too, which is a crucial parameter to be considered in the sensing experiments. Sensitivity can be increased by increasing the number of sensors present in the NV center, that is given by $N = [NV^-]*V$. So, the number of sensors can be increased by increasing the sensor density $[NV^-]$ or diamond volume V.[37] Due to this, the number of photons associated with photoluminescence will also be increased followed by an increase in noise and jitters. As a result, the shot noise limited sensitivity will be less. Also, to excite a large number of sensors, the required laser power will be high too, which can further affect the shot noise. Moreover, if we amplify sensor density keeping the diamond volume constant, it will not be cost-effective, and producing a uniform distribution of sensors will be technically challenging. Apart from that, if the diamond volume is widened, which lowers the spatial resolution and adds imaging difficulties, it is not advisible.

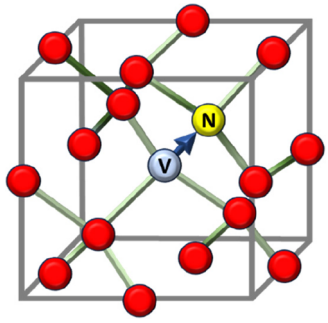

Figure 1. Schematic of the NV structure in a diamond face-centered cubic (fcc) lattice. The carbon atoms in the FCC lattice are represented by the red sphere, the substituted nitrogen atom is depicted by the yellow sphere, and the light blue sphere illustrates the vacancy in the proximity of the nitrogen atom.

In addition to the optically active NV centers, more than 500 different color centers in diamonds have been reported so far.[29,38,39] In recent years, silicon-vacancy (SiV) centers and color centers based on heavier impurities, such as nickel, chromium, and rare earth elements, have been under active research to exploit optical properties. Figure 2 illustrates the important defect centers in diamond and the corresponding absorption wavelengths in the electromagnetic wave spectrum.

3. SYNTHESIS OF DIAMOND

The NV (Nitrogen-Vacancy) center in diamond is a heteromolecular fluorescent lattice defect. It forms when a nitrogen atom is substituted into the diamond lattice alongside a neighboring carbon vacancy. This center, a notable example of a color center, interacts with photons in the visible spectrum. It absorbs light at specific wavelengths, like 532 nm, and emits photons across a broad range, typically between 632 and 800 nm.[40−44] There are mainly two laboratory methods used for the synthesis of diamonds, namely, the high pressure and high temperature method (HPHT method) and the chemical vapor deposition (CVD) method. The HPHT method involves converting a carbon source like graphite under high pressures in the range of 5−10 GPa and a temperature of about 2000 °C, imitating the extreme geological conditions of the natural synthesis of diamonds.[45−47] The CVD diamond synthesis method involves depositing gaseous reactants onto a substrate, offering advantages such as ambient pressure growth and reduced unwanted element incorporation compared with HPHT methods. The process includes reactant flow into the reactor, activation by energy input (via hot filaments or plasma), and subsequent surface reactions on the substrate, leading to diamond film nucleation and growth. Maintaining a substrate temperature of around 800 °C prevents graphite growth, while selective etching by hydrogen atoms promotes diamond

https://doi.org/10.1021/acsomega.4c04406
ACS Omega 2025, 10, 2372−2392

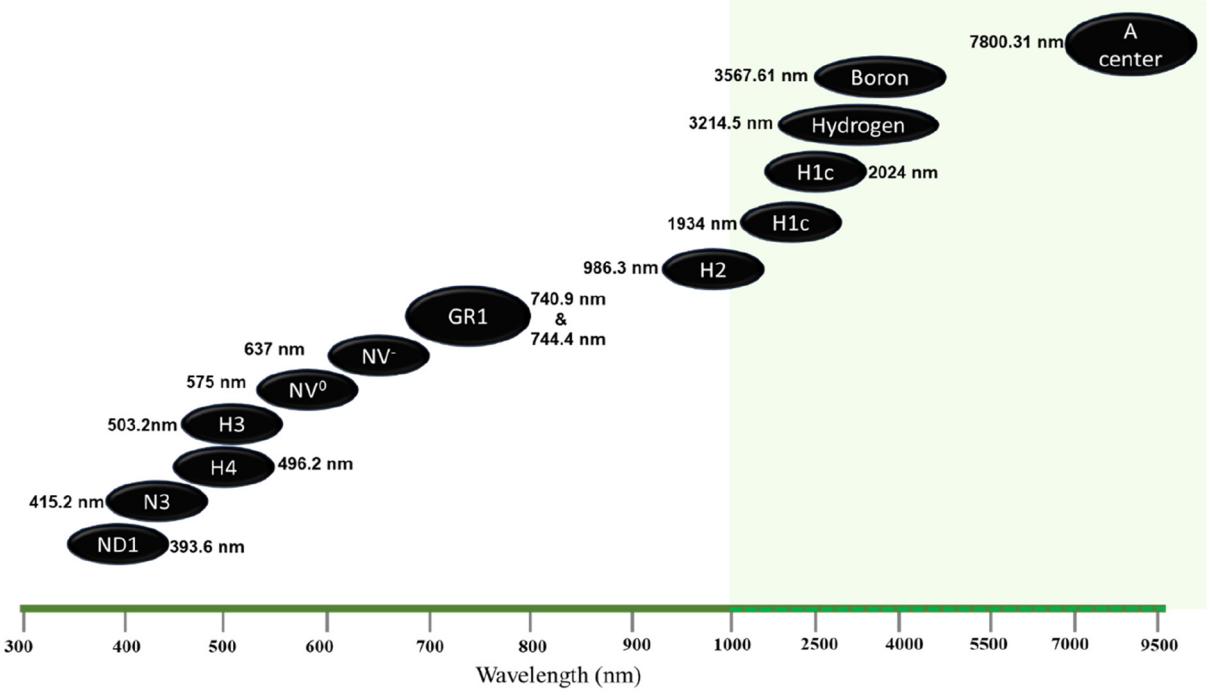

Figure 2. Various optical defect centers in diamond and the corresponding absorption wavelength line.

carbon growth over graphitic carbon.[48−50] Nanodiamonds are produced via a method called detonation, yielding diamond nanocrystals from controlled explosive detonation. Despite their nanometer size, impurities are a prevalent issue in these synthesized nanodiamonds.[51] The NV centers can be formed in diamonds naturally during the laboratory synthesis (for instance, the CVD growth process) of the diamond. It can also be created artificially, by either implanting or irradiating nitrogen into the diamond followed by immediate high-temperature annealing which helps in the migration of carbon vacancies to the proximity of substituted nitrogen impurities.[52−55] Nanocrystalline diamond or nanodiamond (NCDs) has many fascinating properties, based on particle size: nanocrystalline (particle size ∼1 to ≥150 nm), ultra nanocrystalline (∼2 to 10 nm), and diamondoids (∼1 to 2 nm). NCDs find application in emerging areas of power electronics (withstands high current and temperature), field emission (FE: high negative electron affinity), mechanical applications (wear-resistant coatings, lubrication: second hardest material in planet), heat-sinks and heat-spreaders (extremely high thermal-conductivity) and of course nanophotonics, energy, and imaging applications (capable of room temperature single photon generation, detection, and nanoscale magnetometry) toward application in all-solid-state or integrated photonic devices in quantum optics and quantum information).[38,56−60] However, low temperature and commercially viable and industrial synthesis of NCD thin films is still an extremely challenging endeavor. Diamond has extremely slow growth kinetics in low or ambient temperatures further adding to the challenges involved in the nucleation and complex growth steps. While various synthesis methods have been optimized over decades, e.g., detonation; high-pressure-high-temperature (HPHT); chemical vapor deposition (CVD); for low temperature growth of NCD films, plasma enhanced chemical vapor deposition (PECVD) and Pulsed laser deposition (PLD) stands-out. It is evident due to the recent unprecedented advancement of the design modules, materials engineering, microfabrication, and processing technologies that the development of NCD devices is becoming mainstream. Here we will describe mainly two techniques, i.e. plasma synthesis of NCD thin films and PLD deposition of diamond-like carbon thin films.

3.1. Plasma Synthesis of NCD Thin Films. The authors have previously reported extensive studies on the design and development of microwave plasma reactors (MW-PECVD) and tuning of the hazardous high-density plasma and optimization of secondary plasma for low temperatures synthesis of NCDs and related materials (e.g., diamond-like-carbon) with halogenated precursors for photonics and energy applications.[61−69]

The supremacy of microwave PECVD (MW-PECVD) due to its high-density plasma is well established for the synthesis of nonequilibrium NCDs structures from hydrogen diluted carbon-containing precursors.[70] The requirement of high growth temperature (∼700 °C) restricts the application of NCD films in various substrates of commercial significance for microelectronic applications.[71−73] However, MW-PECVD growth of NCD film at low temperature (even room temperature) has been demonstrated with the help of halogenated precursors,[74] interfacial layers (e.g., tungsten),[75] and mechanical seeding procedure,[76,77] or by complicated assembly employing high-frequency linear antennas pulsed MW-PECVD configuration or RF bias in combination with a MW plasma system.[78−80] It is obvious that in nonequilibrium plasma the precursors require some energy threshold for intended growth reactions starting and are conducive in high substrate temperatures.[77] However, the same energetic conditions could be imitated even at much lower temperatures with special arrangements in MW-PECVD.[75] An extensive study has been reported by the authors on the optimization of various process conditions for the low-temperature growth of NCDs employing an indigenously built microwave-plasma

https://doi.org/10.1021/acsomega.4c04406
ACS Omega 2025, 10, 2372−2392

enhanced CVD (MWPECVD: 2.45 GHz, 2 kW) quartz tubular system [Figure 3].[61,62] The effect of deposition

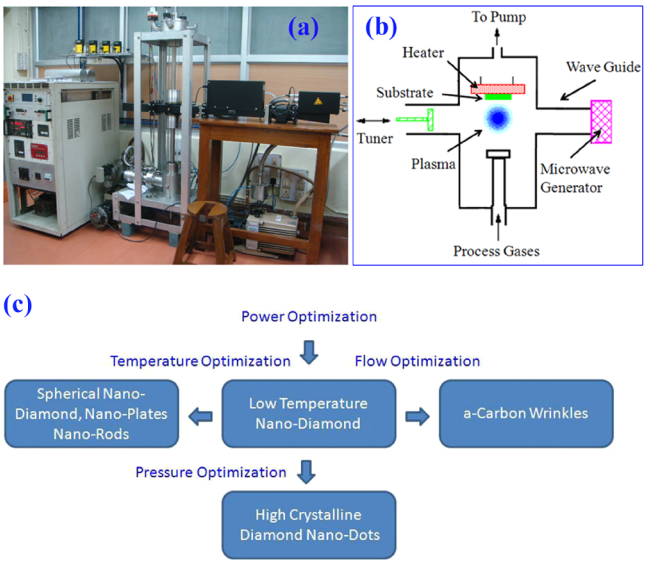

Figure 3. (a) Indigenously built MW-PECVD unit (b) schematic view of the active plasma zone; with (c) the scheme of parameter optimization [reproduced with permission from ref 61].

parameters, e.g., gas pressure (∼10 to 100 Torr), gas flow rate (10−200 sccm), microwave power (100−1500 W), precursors CH_4/H_2 ratio (∼1 to 20), moderate growth temperatures ∼100−400 °C, and deposition time ∼2 and 8 h, with and without seeding layers to act as nucleation centers, has been studied and correlated with microstructural and optical characterizations. While high electrical power evidently aggravates the growth dynamics within plasma precursors, the exposure to direct high-energy ions from the plasma is extremely detrimental for the film growth. Further systematic yet unconventional parametric optimization may be possible with load matching by the reduction in reactor volume, and employing a buffering technique with the help of multiple grid-mask assemblies to mitigate the surface damage by introducing secondary plasma in MW-PECVD, leading to core−shell-like NCD structures (size ∼5−14 nm) with (111) with prominent <111> and <200> crystalline diamond planes (Figures 4 and 5).[68]

3.2. PLD Synthesis of NCDs Thin Films. NCD thin films were deposited by pulsed laser ablation of an HOPG target (SPI Supplies, 444 HP-AB) using a KrF excimer laser (Coherent Inc.) having 20 ns pulse width and 10 Hz repetition rate. Films were deposited on single crystalline SiO_2 (z-cut, one-sided polished, MTI Corp.) substrates, which were cleaned with piranha solution and isopropyl alcohol and jet-dried using high purity (5N) nitrogen gas. The deposition chamber (Excel Instruments) was evacuated to a base pressure of less than 4×10^{-8} mbar, and the films were grown without introduction of any external gas flow. Pulsed laser deposition was carried out at three different experimental conditions by choosing the deposition temperatures to be 500 °C, 700 °C, and room temperature (RT). Now onward, these three samples will be designated as G2, G3, and G1 respectively. The laser fluence was fixed at 3.3 J cm^{-2} and a rotating target carousel ensured uniform ablation. The target-substrate distance was chosen to be 18 cm. For each deposition, 400

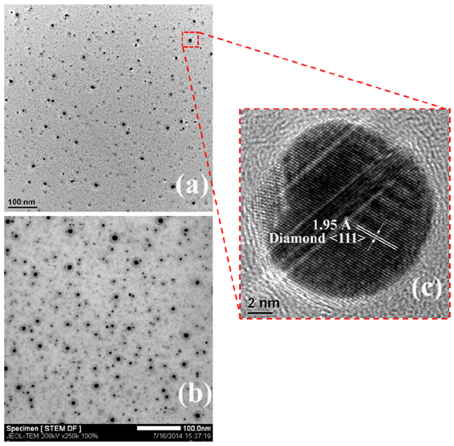

Figure 4. (a) FEG-TEM micrograph for pressure 50 Torr with core−shell structures, in the amorphous network with (b) dark field inverted STEM images identifying different phases of carbon material in core and shell. (c) magnified view of the core demonstrating (111) lattice planes of NCD [reproduced with permission from ref 65.

laser shots were provided to the target. Prior to deposition, a preablation was done by giving 500 shots to the target (while the substrate was covered with a movable shutter). The Raman spectra of the samples are shown in Figure 6 where the G and D peaks can be identified clearly. The position of D peak is around 1333 cm^{-1} revealing the signature of the NCD nature of the thin films, especially for the annealed samples.[81]

3.3. Nanodiamond NV Centers. Nanodiamonds differ from bulk diamonds in several ways: they exhibit greater inhomogeneity due to varied sizes and shapes from the production process. Their specific brightness varies widely but is consistent per unit volume across batches. The quantum yield of NV centers is significantly lower in nanodiamonds, around 50% for bulk crystals. Radiative decay rates are slower in nanodiamonds (8 MHz in water, 3 MHz in air) than in bulk diamonds (44 MHz), and their absorption cross-section is smaller, affecting brightness.[82] Shape and surrounding refractive index notably influence their optical properties, with flake shapes improving radiative rates.[82] Despite these drawbacks, nanodiamonds are valuable in applications like bioimaging and nanoscale temperature measurements due to their small size.[82] Nanodiamonds inherit most of the superior properties of bulk diamonds, and deliver at the nanoscale.[51] The nanometer size requirement for precise sensing and imaging applications can be easily satisfied by nanodiamonds. It typically has shorter T1 relaxation times than bulk diamonds, which can lead to shorter measurement times and more efficient data acquisition.[83] Moreover, the whole purpose of nanodiamond-based sensing is spatial resolution enhanced by nanoscale dimensions. The surface of nanodiamonds can be readily modified to improve their interaction with specific analytes, enabling tailored sensing applications with an increased sensitivity to specific biological or chemical substances. NV-rich nanodiamonds can be functionalized into AFM tips using techniques like focused ion beam (FIB) milling, allowing the creation of customized cantilevers with specific shapes and resonant frequencies for targeted applications.[84] Single nanodiamonds containing a nitrogen-vacancy (NV) center, coupled with an atomic force microscope (AFM), are instrumental in quantitatively mapping stray magnetic fields and studying the nanomechanical properties.[85]

https://doi.org/10.1021/acsomega.4c04406
ACS Omega 2025, 10, 2372−2392

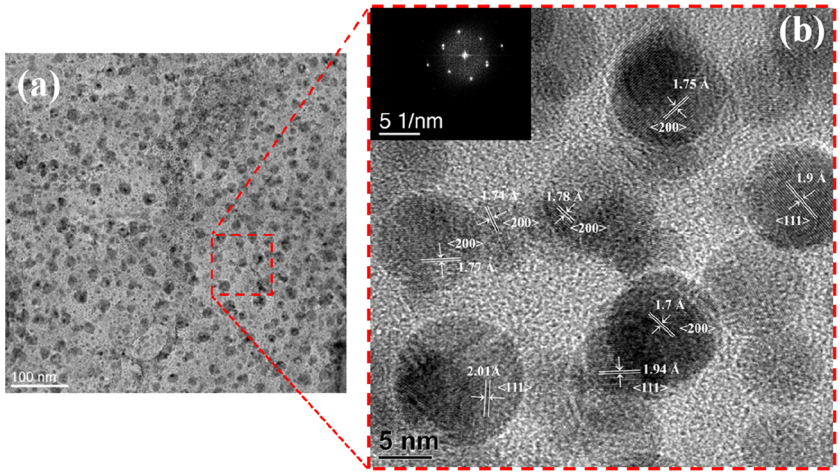

Figure 5. (a) The FEG-TEM micrographs for the optimized NCD grown by secondary plasma. (b) High-resolution image identifying the <111> and <200> diamond planes and FFT pattern [reproduced with permission from ref 65]. Copyright 2015 Elsevier.

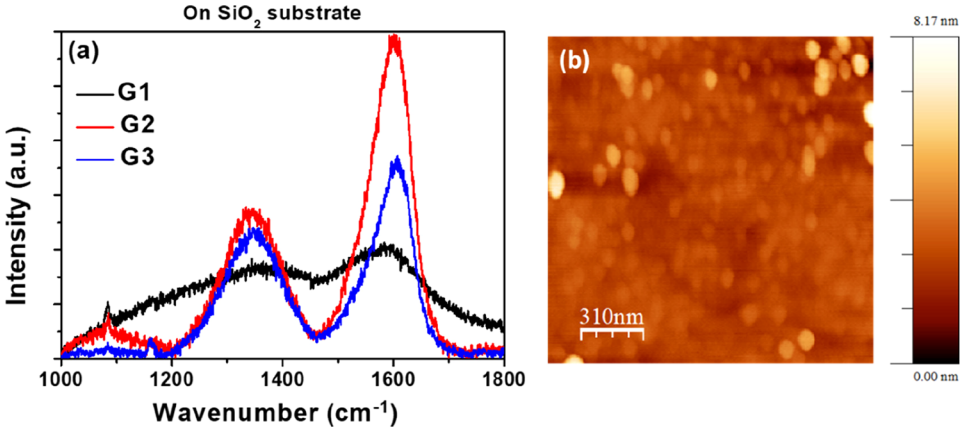

Figure 6. (a) Raman spectra obtained from the films deposited at different substrate temperatures (i.e., G1, G2, and G3). The G and D peaks can be clearly seen. (b) AFM topographic image of G2 sample showing the granular morphology.

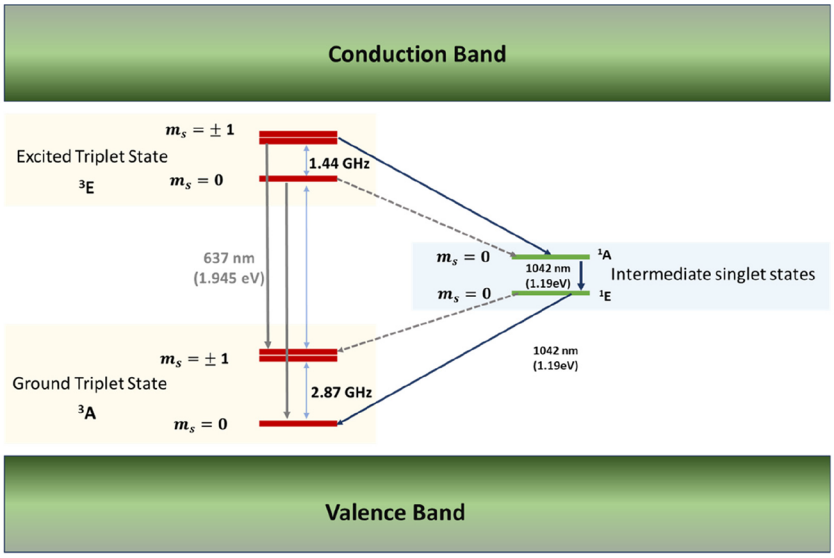

Figure 7. Electronic energy level diagram of the NV center in diamond. The solid gray lines originating from ^3E, $m_s = \pm 1$ (or ^3E, $m_s = 0$) to ^3A $m_s = \pm 1$ (or ^3A $m_s = 0$) correspond to a zero phonon line (ZPL) transition which is radiative emission. The solid blue lines and dotted gray lines illustrate the interstate crossing (nonradiative emission). The nonradiative transitions from ^3E $m_s = \pm 1$ (solid blue lines) are the highest probable compared to the transition from ^3E $m_s = 0$ (dotted gray lines).

https://doi.org/10.1021/acsomega.4c04406
ACS Omega 2025, 10, 2372−2392

In addition, Kewes et al. have demonstrated a pick-and-place of nanodiamonds which can be employed in developing an integrated quantum sensor.[86]

4. ELECTRONIC STRUCTURE OF NV CENTERS

It has been found that such formed NV center exists in four different charge states, NV^{+1}, NV^{0}, NV^{-1}, and NV^{-2}.[87] NV^{0} centers, neutral nitrogen-vacancy defects, have a nitrogen atom next to a vacancy in the diamond structure without an extra electron. On the other hand, NV^{-} centers, which are negatively charged nitrogen-vacancy defects, contain an additional electron at the defect site, making them negatively charged. The −1 charge state is a more stable form than the −2 and +1 states. The difference in charge greatly affects how NV centers behave and what they can be used for. NV centers show great potential for things like quantum sensing, single photon emission, and magnetometry because of how they interact electronically and optically. On the other hand, NV^{0} centers are getting noticed for their potential in quantum computing, biosensing, and imaging at the nanoscale.[88] The NV^{-} c-centers contain a total of six electrons; four of them pair up with 3 carbons and a vacancy, and the remaining two unpaired electrons make spin-triplet states at the ground state level.[89] The NV center encompasses two primary groups of quantum states: the ^{3}A-triplet ground state and the ^{3}E-triplet excited state. The spin triplets experience zero-field splitting, resulting in their division into two distinct sets of nondegenerate spin sublevels: one with zero spin ($m_s = 0$) and two with spins of $m_s = \pm 1$. This splitting, driven by the interplay of crystal field effects and spin−spin interactions, manifests as a separation of approximately 2.87 GHz between the ground state triplet states (^{3}A) and a separation of 1.42 GHz between the excited triplet state (^{3}E)[87] (Figure 7). In addition to the aforementioned triplet states, there exist intermediary singlet states (^{1}A and ^{1}E) positioned between them, serving a crucial function in the nonradiative decay processes occurring between the triplet states.[90,91] We focus on the magnetic field applied along the N−V (nitrogen-vacancy) axis because the energy levels of the nitrogen-vacancy center in diamonds are highly sensitive to magnetic fields aligned with this axis. When a magnetic field is applied along the N−V axis, it causes Zeeman splitting specifically of the $m_s = \pm 1$ sub levels. This is due to the magnetic interaction with the NV center's spin state.[92] The NV center has a high degree of symmetry along the N−V axis. The electronic structure of the NV center is such that the axis connecting the nitrogen atom to the vacancy plays a special role in determining the electronic states. Magnetic fields aligned with this axis interact strongly and predictably with the NV center's spin states. The interaction between the magnetic field and the NV center's spin states is maximized when the field is aligned with the N−V axis. This makes the observation and manipulation of the spin states easier, which is crucial for applications in quantum information and sensing. Apart from other ODMR frequencies, when a magnetic field is not aligned with the N−V axis, it can be decomposed into components parallel and perpendicular to the N−V axis. Only the parallel component directly contributes to the Zeeman splitting of the $m_s = \pm 1$ states. The perpendicular component, however, can induce transitions between the spin states, resulting in more complex behavior. The spin states $m_s = 0$ and $m_s = \pm 1$ remain good quantum numbers as long as the two dominant terms in the Hamiltonian, zero-field splitting (H_{ZFS}) and Zeeman splitting (H_{Zeeman}), share the same principal axis.[93] Misalignment leads to spin state mixing and reduces the ODMR contrast, an effect that worsens with increasing magnetic field strength B_0.[94] Moreover, nanodiamonds exhibit a slight decrease in T_2 (transverse spin coherence time) compared with bulk diamonds. However, T_2 can be further reduced if there is a misalignment in the magnetic field.[95] T_2 measures how long the spins in nitrogen-vacancy (NV) centers in diamond stay coherent. This is crucial for quantum information processing and precise magnetic measurements. NV center's electronic spin can maintain its coherence better when the magnetic field is aligned with its axis, as it minimizes certain decoherence mechanisms.[95]

When the magnetic field is not aligned with the NV axis, the coherence time T_2 exhibits a significant reduction. This reduction arises from the interaction between the electronic spin of the NV center and the surrounding bath of ^{13}C nuclear spins. The misalignment interrupts the usual cancellation of dipolar field contributions from the ^{13}C nuclei, which typically occurs when the magnetic field is properly aligned with the NV axis. Consequently, the NV spin undergoes accelerated decoherence, driven by fluctuations in the hyperfine interaction with the ^{13}C spins.[95] Walsworth et al. have demonstrated that the decoherence for the Hahn-echo signal (a method used to measure spin coherence) of an individual NV center is exponential, with a decay rate that depends on the angle of misalignment and the strength of the hyperfine interaction with the nearest ^{13}C nuclear spin. That is, even a slight misalignment can significantly reduce the coherence time.[95]

Irrespective of misalignment or not, in principle to induce coherent spin excitations, allowing the NV center to exist in a quantum superposition of $m_s = 0$ or $m_s = \pm 1$, an electromagnetic wave is utilized for excitation.[89,96] Specifically, a microwave pulse is necessary, as the energy gap between the states falls within the GHz frequency range of electromagnetic radiation.[90]

4.1. Energy States and Hamiltonian.

The overlapping of sp^3 orbitals among carbon atoms in diamonds results in valence and conduction bands characterized by an energy gap of 5.47 eV.[97] Within this gap, energy states induced by impurities are situated. As mentioned above, the electrons in the vacancy center can aggregate into two states, characterized by spin values of $S = 1$ and $S = 0$, representing the triplet and metastable singlet states, respectively. In both configurations, excited and ground states are present within the bandgap. Specifically, the triplet states are labeled as ^{3}E (excited) and ^{3}A (ground) with the highest separation of 1.96 eV, while the singlet states are identified as ^{1}E and ^{1}A with a separation of 1.19 eV[91] (Figure 7).

A deeper look into the Hamiltonian of the NV center is needed for a better understanding of the electronic structure as the vacancy center does not possess a simple two energy levels. In one of the models, the Hamiltonian consists of mainly 4 terms: Zero-field splitting ($\mathcal{H}_{zf}$), the electron-Zeeman interaction ($\mathcal{H}_Z^e$), hyperfine coupling ($\mathcal{H}_{hf}$), and nuclear Zeeman interaction ($\mathcal{H}_Z^N$),[33,98]

$$\mathcal{H} = \mathcal{H}_{zf} + \mathcal{H}_Z^e + \mathcal{H}_{hf} + \mathcal{H}_Z^N \quad (1)$$

$$\mathcal{H} = \vec{S}^T \overline{D} \vec{S} + \gamma_e \vec{S}\cdot\vec{B} + \vec{S}^T \overline{A} \vec{I} - \gamma \vec{I}\cdot\vec{B} \quad (2)$$

$\overline{D}$ is the zero-field tensor, $\overline{A}$ is the hyperfine tensor, and S and I are the electronic and nuclear spin operators, respectively.[98]

https://doi.org/10.1021/acsomega.4c04406
ACS Omega 2025, 10, 2372−2392

The aforementioned zero field splitting term ($\mathcal{H}_{zf}$) gives rise to a splitting of the NV spin $m_s = 0$ and $m_s = \pm 1$ sublevels in the absence of a magnetic field.[89] This behavior is primarily influenced by the zero-field tensor $\bar{D}$, which exhibits a linear temperature dependence of −70 kHz/K within the temperature range of 280 to 330 K.[33,99,100] This property can be leveraged to employ NV centers as nanoscale temperature sensors.[100] The Zeeman term ($\mathcal{H}_Z^e$) results from the interaction of the spin with the external magnetic field.[41] When the field is aligned with the NV axis, the degeneracy of $m_s = \pm 1$ in both ^{3}A and ^{3}E will be lifted as a function of field strength. For a very large off-axis field, m_s will not be a good quantum number anymore, and it will lead to the inefficient spin-dependent photoluminescence of the NV center.[101] The third term, hyperfine coupling ($\mathcal{H}_{hf}$), is primarily due to the nitrogen (^{14}N) nucleus which has nuclear spin $I = 1$, interacting with the NV electronic spin.[102,103] In the presence of a magnetic field, I splits into $2I+1$ number of sublevels, which corresponds to the fourth interaction term nuclear Zeeman interaction ($\mathcal{H}_Z^N$). Both the nuclear Zeeman interaction and hyperfine coupling terms do not change the electronic states much; nonetheless, they play a significant role in the interaction between the NV spin qubits.[98]

4.2. Optical Transitions and Optical Spin Polarizations. Figure 7 illustrates the optical spectra of a single NV center which contains a broad absorption band and a broad emission band. Due to the interactions of electronic and vibrational states, the most probable transitions at thermal equilibrium are those from the lowest vibronic levels of the ground state to the higher levels of the excited state which gives out an absorption band peaking around 560 nm called the Phonon Side Band (PSB).[33,50,104] The NV center can be excited in a spin-conserving transition from ^{3}A to ^{3}E through the application of laser at 532 nm.[90] The transitive decay to all the vibronic levels in the ground state follows after that and gives rise to emission PSB ranging from 637 to 750 nm.[33] Zero phonon line (ZPL) at a wavelength λ_{ZPL} = 637 nm corresponds to the emission process when there is no conversion of energy through phonon-assisted vibrations.[105]

There is an alternative nonradiative pathway (releasing heat by the vibrations of the diamond lattice) through which the NV center decays from ^{3}E to ^{3}A state without spin conservation, called intersystem crossing. Thus, the spins relax from ^{3}E to one of the metastable singlet states (^{1}E), followed by the radiative decay to ^{1}A with the emission of a photon of wavelength 1042 nm (Figure 7) and finally reaches back to ground triplet state ^{3}A. The spins $m_s = \pm 1$ in the excited state ^{3}E are more likely to decay through the above-mentioned path.[90] Moreover, the probability of nonradiative decay from ^{1}A to $m_s = 0$ spin in ground state ^{3}A is more than to spin $m_s = \pm 1$. Hence there will be less fluorescence if the NV center is excited into the $|\,^3\mathrm{E}, m_s = \pm 1\rangle$ state in the first place. Similarly, if the spin was already in $|\,^3\mathrm{E}, m_s = 0\rangle$, the electrons in the NV center would preferably give out a spin-conserving fluorescence emission by decaying to the $|\,^3\mathrm{A}, m_s = 0\rangle$ spin state. This spin-state-dependent decay from ^{3}E to singlet states to $m_s = 0$ sublevel in the ^{3}A produces the optical spin polarization in the ground state. In the transition from the $|\,^3\mathrm{E}, m_s = 0\rangle$ to $|\,^3\mathrm{A}, m_s = 0\rangle$ state, the fluorescence emission is approximately 30% greater compared to transitions between the $|\,^3\mathrm{E}, m_s = \pm 1\rangle$ and $|\,^3\mathrm{A}, m_s = 0\rangle$.[105] This variation in the intensity of fluorescence provides the optical contrast necessary to perform the so-called Optically Detected Magnetic Resonance (ODMR).[33,106]

5. MAGNETIC SENSING

Diamond-based quantum sensors, particularly NV centers, have become increasingly popular due to their ability to use spin-dependent photoluminescence to detect time-resolved weak magnetic fields at ambient temperatures with high spatial accuracy and field sensitivity. In addition to their primary use in magnetic field measurement, NV centers can also be employed to sense other factors, such as electric fields, temperature, and pressure. Additionally, compared to conventional scalar magnetometers, which are limited to measuring only the magnitude of magnetic fields along a single direction, the NV center can also be used as vector magnetometry. This capability not only enables the measurement of the magnetic field's strength but also ensures that the orientation of the sensing element remains constant relative to the applied field direction. Consequently, the sensor accurately detects the projection of the field along its symmetry axis. This versatility makes them valuable for a wide range of applications in scientific research and technology. The fundamental principle of magnetic field sensing for an NV center is rooted in the Zeeman shifts, which describe the splitting of spectral lines when exposed to an external magnetic field. This shift in energy levels can be measured and used to detect and quantify the strength of the magnetic field.

There exist multiple techniques for detecting magnetic fields, commonly referred to as magnetometry. These techniques involve the use of different types of sensors,[107,108] such as GMI (Giant-magneto impedance), magnetoelectric,[109,110] Hall effect, Fluxgate,[111−113] DC SQUIDs (Superconducting Quantum Interference devices),[114] cavity optomechanical,[115−117] AMR/GMR/TMR (Anisotropic/Giant/Tunneling magnetoresistance),[118−121] and others.

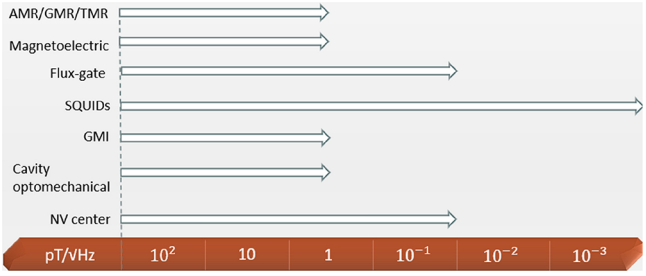

Figure 8. Comparison of different magnetic field sensors based on sensitivity.

GMI was introduced approximately three decades ago (around the 1990s) and has a sensitivity of around 1×10^{-12} T/$\sqrt{\text{Hz}}$. Other sensors such as cavity optomechanical, magnetoelectric, and magnetoresistance sensors exhibit sensitivity around the pT/$\sqrt{\text{Hz}}$ range.[109,110] SQUIDs and optically pumped sensors on the other hand are capable of reaching the femto-tesla threshold but require cryogenic cooling.[122] For the characterization of magnetic field sensors, field sensitivity and spatial resolution matter most, but also other parameters like sensor size, response time, power consumption, temperature dependency, and linearity should be taken under consideration. From this perspective, it is evident that numerous weak magnetic field sensors are accessible; however, the selection of sensors depends on the

https://doi.org/10.1021/acsomega.4c04406
ACS Omega 2025, 10, 2372−2392

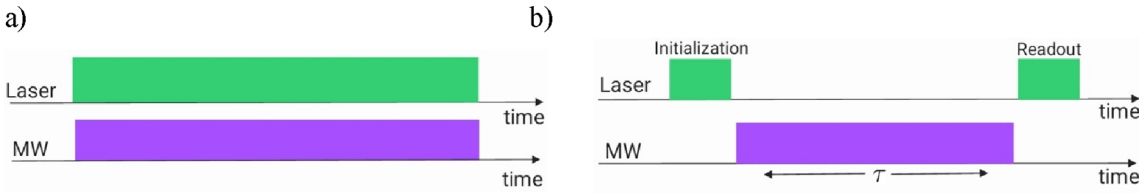

Figure 9. ODMR methods. a) CW-ODMR, b) pulsed ODMR.

specific application at hand. For an NV center, the most important parameter is its performance at room temperature. While usually in CW-ODMR, the NV center sensitivity lies around nT/$\sqrt{\text{Hz}}$, and there is room to improve the sensitivity by introducing pulsed-ODMR (Rabi and Ramsey methods), selecting appropriate imaging techniques, enhancing the readout fidelity, and eliminating noise sources like laser intensity fluctuations, phase noise, thermal noise to achieve subpico tesla range.[122] In their report, Wolf and his co-workers have demonstrated that subten pico tesla sensitivity could be achieved inducing different pulsing schemes and eliminating noise sources like laser fluctuations, phase noise, thermal noise, and readout fidelity. However, in the original published paper, they mentioned a sensitivity value of 0.9 pT/$\sqrt{\text{Hz}}$. Subsequently, the same group has included an erratum to justify their overestimated value of sensitivity by an order of magnitude. The error originated from the averaging over a measurement time of 100 s, which was wrongly considered during the calculation of Allan deviations. This led to an error of $\sqrt{100} = 10$ times. It may be noted that in recent works flux concentrators have been used to achieve a sensitivity of the subpico tesla range. However, Fescenko et al. have reported sensitivity values of 0.9 pT/$\sqrt{\text{Hz}}$ in diamond magnetometry using a 200 mW laser by employing ferrite flux concentrators.[123,124]

5.1. DC and AC Magnetic Sensing. Quantum sensing utilizing an NV center can be classified into two primary categories: AC magnetometry (identification of narrowband time-varying signals, typically at frequencies around 10 MHz) and DC magnetometry (detection of broadband DC signals or magnetic fields changing gradually). The DC sensing methodology primarily considers utilizing two distinct techniques: CW-ODMR (Continuous-Wave Optically Detected Magnetic Resonance) and Pulsed-ODMR employ both π-pulse and Ramsey sequences. On the other hand, a sophisticated Ramsey magnetometry approach denoted as an Echo sequence (alternatively recognized as Han-echo or Spin−echo) is utilized for AC sensing. Some essential parameters that govern the sensitivity are named dephasing time T_2^*, coherence time T_2, spin relaxation time T_1, and detuning factor $\Delta\nu$.

Moreover, the sensitivity of both AC and DC mechanisms depends on several variables, including the diamond size (whether it is nanodiamond or bulk), the characteristics of NV centers (whether they're single or in an ensemble), and their positioning (whether they're on the surface or internally embedded). Furthermore, resonant optical and microwave excitation, readout techniques, and an imaging approach radically influence the sensitivity of the overall system.

Thus, when dissecting the fundamental pillars contributing to the sensitivity of NV centers, we can identify five key parameters: Diamond Structure, Optical Excitation, MW Field, Readout Finiteness, and Imaging Techniques. Each of these pillars plays a vital role in shaping the sensitivity and effectiveness of NV center-based quantum sensing.

5.2. Microwave Control. The precise manipulation of the microwave (MW) field's coherence (coherent MW control) stands out as a crucial factor in harnessing the NV center's potential as a quantum sensor. In conventional ODMR for an NV center, the population is transferred from the $m_s = 0$ to $m_s = \pm 1$ state in the $^3A_2$ multiplet with a resonant MW frequency of 2.87 GHz (D_{gs}). This whole picture of NV spin can be demonstrated geometrically using a Bloch sphere where the population of $m_s = 0$ is, and the $m_s = -1$ state represents the two-level system along the z-direction, and the azimuthal angle represents the phase. In simple terms, if the applied magnetic field is at a resonant frequency along the z direction, the NV electron spin state vector coincides with the direction of the exerted magnetic field.

The sensitivity of an ensemble of N spins in a diamond for a Ramsey magnetometry is given by,

$$\eta_{\text{Ramsey}}^{\text{ensemble}} \approx \frac{\hbar}{\Delta m_s g_e \mu_B} \frac{1}{\sqrt{N\tau}} \frac{1}{e^{-(\tau/T_2^*)^p}} \sqrt{1 + \frac{1}{C^2 n_{\text{avg}}}} \sqrt{\frac{t_I + \tau + t_R}{\tau}} \tag{3}$$

where $\frac{\hbar}{\Delta m_s g_e \mu_B} \frac{1}{\sqrt{N\tau}}$ signifies the spin projection limit, $\frac{1}{e^{-(\tau/T_2^*)^p}}$ is the spin dephasing, $\sqrt{1 + \frac{1}{C^2 n_{\text{avg}}}}$ defines the readout, and $\sqrt{\frac{t_I + \tau + t_R}{\tau}}$ represents the overhead time.[125]

5.3. Continuous Wave ODMR. Continuous wave ODMR is one of the most popular and frequently implemented approaches for observing photoluminescence spectra, where the optical excitation and the MW field are applied in parallel. Due to continuous green laser excitation, the NV center spins populate at the $m_s = 0$ state; however, the ongoing resonant MW shifts the spins at the less fluorescent $m_s = \pm 1$ state, resulting in a dip in the resonant frequency in the fluorescence spectra.

The sensitivity of the CW-ODMR procedure is given by,

$$\eta_{\text{CW}} = \frac{4}{3\sqrt{3}} \frac{h}{g_e \mu_B} \frac{\Delta\nu}{C_{\text{CW}}\sqrt{R}} \tag{4}$$

where, g_e is electrons gyration factor, μ_B is the Bohr magneton, C_{CW} represents the continuous-wave contrast, R is the photon detection rate, and $\Delta\nu$ is the frequency detuning.[125]

When it comes to high-sensitivity applications, CW-ODMR is not advised because of poor sensitivity (around μT/$\sqrt{\text{Hz}}$). Yet, the application of pulsed magnetometry (using Ramsey or Han-echo sequence), pulsed laser, or AOM (Acousto Optic Modulator) excitation, beam shaping, and improvement in spin readout methods can enhance the sensitivity even further.

5.4. Pulsed ODMR. As discussed, the transition of spin population can be driven with continuous excitation in CW-ODMR, and to increase the sensitivity, a pulsed approach of

https://doi.org/10.1021/acsomega.4c04406
ACS Omega 2025, 10, 2372−2392

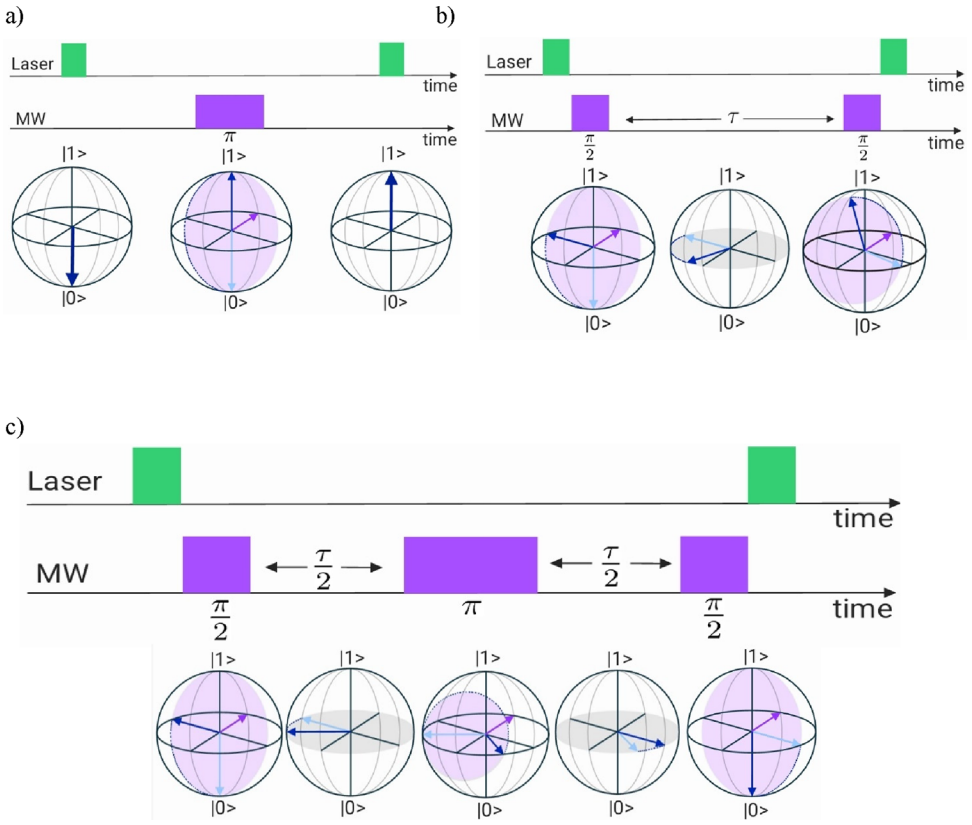

Figure 10. Various pulsed ODMR approach. a) π pulsed and b) Ramsey magnetometry for DC field sensing, c) Hahn-echo sequence for AC magnetometry.

resonant MW is applied. If $m_s = 0$ and $m_s = -1$ states are two poles considered as $|0\rangle$ and $|1\rangle$ simultaneously in the Bloch sphere along the z direction, a π-pulse rotates the NV spin around the x or y axis in the xy-plane inverting the population from $|0\rangle$ to $|1\rangle$ and vice versa, whereas a $\pi/2$-pulse causes a rotation transferring the spin population on the $x-y$ plane, preparing a superposition state. To determine the time scale of MW pulse duration (π and $\pi/2$-pulse), it is necessary to measure the Rabi frequency (Ω_R). A feedback approach is used to calculate the Rabi frequency where the NV spin population is initialized at the $|0\rangle$ state, with constant amplitude MW and duration τ and measuring the photoluminescence. The steps are repeated with various τ values each time. As a result, information about the exact time duration to rotate the spin, half (π-pulse), and quarterly ($\pi/2$-pulse) rotations on the Bloch sphere can be obtained.

In conventional pulsed magnetometry, pulsed MW is applied in the absence of optical excitation. For instance, an initial laser pulse of very short duration is applied first, followed by the MW excitation pulse and finally with a readout optical pulse. It is recommended that multiple measurements of the readout data be taken to ensure optimal control.

However, commonly two main approaches are considered in pulsed magnetometry; π-pulse and Ramsey sequence. The π-pulse reduces the fluorescence maximally while rotating the spin from the $m_s = 0$ to $m_s = -1$ state. On the other hand, the traditional Ramsey sequence is slightly different compared to π-pulse where initially a $\pi/2$-pulse is applied that rotates spin on the xy-plane. Here, the spin state precesses on the azimuthal plane, driven at the detuning frequency $\Delta\nu$ for a duration of τ. After that, another $\pi/2$-pulse turns the spin (with the extra phase obtained for the period τ) completing a total π rotation, followed by the readout pulse.

In Ramsey magnetometry, as the extra phase information, obtained due to precession on the xy-plane, increases parallel with the sensing interval τ, the overall sensitivity increases. Compared to CW-ODMR, Ramsey measurement offers better accuracy in measuring magnetic sensitivity but is limited by the dephasing time, T_2^*.

The sensitivity for a Ramsey-type NV center ensemble is given by,

$$\eta_{\text{Ramsey}}^{\text{ensemble,shot}} \approx \frac{\hbar}{\Delta m_s g_e \mu_B} \frac{1}{\sqrt{N\tau}} \frac{1}{Ce^{-(\tau/T_2^*)^p}} \sqrt{\frac{t_I + \tau + t_R}{\tau}} \tag{5}$$

where t_I is spin initialization time, τ precession time, t_R measures the readout, and C is contrast, which, in a reduced way, shot -noise-limited Ramsey sensitivity is expressed as,

$$\eta_{\text{pulsed}} \approx \frac{8}{3\sqrt{3}} \frac{\hbar}{g_e \mu_B} \frac{1}{C_{\text{pulsed}}\sqrt{N}} \sqrt{\frac{t_I + T_2^* + t_R}{T_2^*}} \tag{6}$$

When it comes to AC magnetometry,[1,126] a specialized Ramsey sequence, Hahn-echo, or spin-echo is implemented where in addition to Ramsey, an additional π-pulse is applied in between the $\pi/2$-pulses followed by τ duration, which on another note increases the sensitivity even further. All of these pulse-modulated MW signals are delivered with the help of IQ modulation. An essential shortcoming of CW and pulsed ODMR methods is that both are constrained by the coherence time T_2 and dephasing time T_2^*. Other advancements like

https://doi.org/10.1021/acsomega.4c04406
ACS Omega 2025, 10, 2372−2392

dynamical decoupling[127−129] and spin-bath[130,131] driving can also be applied further to cope with these shortcomings.

While CW ODMR is primarily used for DC magnetometry, the purpose of using pulsed ODMR is for AC sensing. Looking at the advantages of CW-ODMR, it is the most convenient approach in NV sensing, where the laser and the MW excitation are applied simultaneously. Compared to the pulsed approach, it is easy to implement because there is no pulse technique involved. Despite the simplicity, continuous wave ODMR suffers from some disadvantages also. The continuous laser and microwave excitations deteriorate the measurement sensitivity. The readout fidelity is not that good. The fluorescent line width is much broader. Apart from that, they also suffer from optical and microwave power broadening.

However, pulsed ODMR has its advantage in terms of sensitivity. The protocol involves providing a laser pulse for initialization, followed by a MW π-pulse and a laser readout pulse. With the appropriate Rabi frequency, the pulsed method provides better sensitivity compared to CW-ODMR. Also, a decreased line width can be achieved.

In Ramsey magnetometry, a sophisticated pulse technique is used, where the NV-spin freely precesses in the absence of laser and MW excitation, acquiring a phase due to interaction with the external magnetic field. This is achieved by providing a precession time between two $\pi/2$ − MW pulses. By varying the precession time interval and taking multiple readings, it is possible to determine the external field from multiple phase accumulated signals. The Ramsey technique is more efficient instead of pulsed and continuous wave due to its flexibility to adopt other methods like spin−echo and decoupling sequences to optimize the dephasing in AC magnetometry.

There is a chance of environmental perturbations during free precession in Ramsey magnetometry. So, to avoid that, a π-pulse is embedded in the middle of two $\pi/2$ − MW pulses in the Hahn Echo or Spin Echo sequence. Due to this, the dephasing time exceeds the decoherence time, which in this case improves the sensitivity for AC magnetometry. It is also possible to detect a higher frequency ac magnetic field with the Carr−Purcell−Meiboom−Gill (CPMG) protocol where more than one π-pulses are introduced like the Ramsey method. It may be noted that the sensitivity also depends on the diamond size (bulk or nanodiamond), single or ensemble of the NV center, NV center position (on the diamond surface or inside).

Table 1. Magnetic Field Sensitivity Based on Various Protocols in DC and AC Magnetometry

Protocols	Sensitivity to B in parallel to NV axis with typical frequency	Typical Sensitivity
CW-ODMR	10^3−10^1 Hz	μt−nT/$\sqrt{\text{Hz}}$[125,132]
Ramsey	10^5−10^3 Hz	μt−nT/$\sqrt{\text{Hz}}$[125,132]
Echo sequence	10^6−10^3 Hz	nt−pT/$\sqrt{\text{Hz}}$[38,125,132]
CPMG	10^7−10^4 Hz	nt−pT/$\sqrt{\text{Hz}}$[125,132,133]

5.5. Optical Excitation of NV Color Centers. To excite the NV centers, a 532 nm green laser is applied with some intensity. Therefore, with an increase in intensity, there is a higher probability of electrons to jump from the $^3A_2$ state to 3E state quickly. This relation is given by, $\Gamma = I\sigma$, where, the optical pump rate Γ represents the probability of absorption by the NV center from the cross-section area σ.[134,135] After excitation, the spins decay either by radiative or by non-radiative. There are multiple factors in optical excitation (frequency modulation, pulsed laser source, and beam shaping) that can be introduced to improve the sensitivity of the sensor.

5.5.1. Acousto-Optic Modulation. Using the AOM, we can modulate the frequency and intensity of the laser. Also, for pulsed based ODMR, initialization and readout pulses are provided for excitation and data acquisition with a time delay. It is useful to use AOM to generate a pulsed output. So, including AOM in the experimental setup for NV magnetometry can be beneficial as pulsed sensing delivers better sensitivity rather than continuous wave.

5.5.2. Beam Shaping. When a laser is applied to the sample, the laser intensity is not equally distributed all over the beam width. Usually, laser intensity has a Gaussian distribution, which clearly shows that it has an inhomogeneous distribution over the sample. For ensemble magnetometry, if the applied laser is homogeneously spread over the sample, it is seen that the homogeneity predominantly improves the overall signal-to-noise ratio (SNR).[136]

5.5.3. Readout Fidelity. The photoluminescence is converted into electrical signals for counting by SPADs, which basically convert photon energy into electrical signals. But there is no surety that photons impinging on the detector are actually absorbed and converted into electrical signals. This is known as the shot noise. Also, to get an adequate readout, it is extremely necessary to get satisfactory count rates for a sufficiently good signal-to-noise ratio (SNR). So, readout fidelity basically explains how fast we can read our experimental data without introducing noise. Multiple techniques can be used to mitigate the noise sources like lock-in-detection and CMR (common mode rejection for laser noise), improving the detector quality and imaging processes. Different readout methods like spin-to-charge conversion (SCC) readout,[125] photoelectric readout, and level-ant crossing-assisted readout can be obtained which helps to increase the readout fidelity.

6. IMAGING TECHNIQUES

While there are multiple imaging mechanisms existing, practically some of them are to be considered important, particularly in NV sensing, widefield magnetometry, and scan probe magnetometry. Widefield is most commonly used, whereas scan-probe is the most complex approach at this time providing a spatial resolution of around 50 nm. Below each of the imaging methods, it is briefly explained.

6.1. Widefield Imaging. The widefield approach typically shows a spatial resolution of about 400 nm, and it is commonly used in diamond magnetometry.[136] A key advantage of using widefield if applied in ensembles of NV centers shows much better sensitivity.[137,138] In this method, the NV center ensembles on the diamond surface are excited with a green laser, and the surface is imaged with a CCD camera simultaneously. The 3D magnetic field captured from the surface can be utilized as vector magnetometry, which is another advantage of widefield imaging. The images can be improved with pulsed MW and employing spin−echo sequences. Furthermore, with the help of decoupling, dephasing can be improved with the sensitivity acquired around nT/$\sqrt{\text{Hz}}$.

Some of the primary specifications of using widefield imaging with an ensemble of NV centers can be listed as high spatial resolution, field sensitivity, and vector magneto-

https://doi.org/10.1021/acsomega.4c04406
ACS Omega 2025, 10, 2372−2392

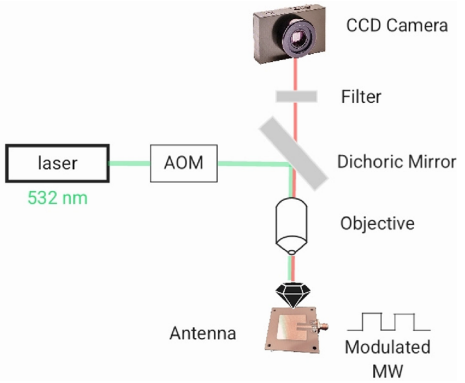

Figure 11. Schematic of experimental setup for widefield magnetometry.

metry which makes widefield ensemble magnetometry ideal for bioimaging applications, MRI, and microscopic imaging.[139,140]

6.2. Scanning-Probe Magnetometry. Scan-probe magnetometry is one of the most sophisticated techniques which even surpasses the so-called confocal imaging because of its ability to probe magnetic fields.[141,142] To achieve a good spatial resolution, the NV center must be on the surface of the diamond sample, which is achievable with different available techniques. However, the main problem faced during widefield is the optical diffraction limit that keeps the resolution within bounds, whereas in scanning, it is possible to overcome this with the help of AFM (atomic force microscopy) which further increases the resolution. Here the sample is attached to the AFM tip so that the spatial resolution can be achieved with proximity, sometimes the a scanning distance of >100 nm in nanodiamonds from the surface. Moreover, when applied to nanodiamond magnetometry, some drawbacks on single NV can be seen due to the short coherence time and instability on the surface. However, some recent publications claim scanning magnetometry based on monolithic diamond nanopillars with single NV centers shows much better sensitivity.

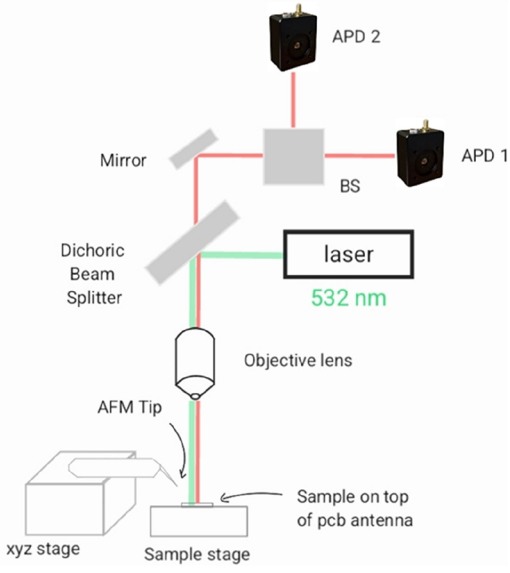

Figure 12. Schematic of scanning-probe magnetometry.

Also scanning magnetometry can be implemented to pursue further research on other parameters like charge transports and high-temperature sensors.[20,92]

As we indulge in a brief discussion about different imaging techniques, it is always advisible to select the imaging technique properly based on our application suitable for it. There are always ways to improve the field sensitivity and spatial resolution to get genuine data, and a proper survey should be done from available research ensuring tools and techniques, methodologies, and effectiveness before jumping into the application.

7. DIAMOND COLOR CENTERS FOR ENERGY APPLICATIONS

Describing all of the applications of nitrogen vacancy centers in diamond is beyond the scope of the present review. Thus, in this article, we focus mainly on the energy-related applications of diamond-based sensors having optically addressable defects. From the existing literature, we have categorized three major emergent sections where various properties of diamond-based sensors could be exploited, viz. (i) oil and gas industry, (ii) battery research, and (iii) photovoltaics.

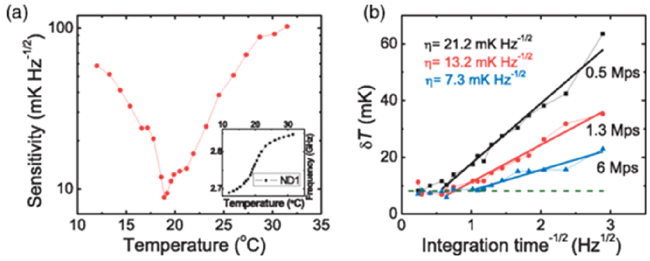

Figure 13. Sensitivity of a magnetic criticality enhanced Gd-FND temperature sensor. (a) Sensitivity of the hybrid sensor at various temperatures. The red dots are the sensitivity determined by equation (a2) using the experimentally measured photon counts, ODMR contrast, $d\omega/dT$ and spin resonance width $\Delta\omega$. The laser power is chosen such that the photon count is ≈6 Mps. The optimal sensitivity ≈7.3 mK/$\sqrt{\text{Hz}}$ is achieved at TC = 19 °C. Frequency shift of the Gd-FND sensor as a function of temperature under an external magnetic field of 100 G. (b) Standard deviation of temperature measurement as a function of the data acquisition time for various photon counts (due to different laser powers) using the three-point method. The slopes of the curves give the shot-noise-limited sensitivity of the hybrid sensor. The green dashed line corresponds to the temperature stability of the incubator. Adapted from ref 148. Published by the American Physical Society under the terms of the Creative Commons Attribution 4.0 International license.

7.1. Oil and Gas Industry. Oil and gas (exploration) industries use various sensors to acquire subsurface data, which is helpful in predicting the nature and capacity of the reservoir. Apart from subsurface exploration, multimodal sensors are used in long pipelines to transport oil and gas. These sensors are used to maintain the integrity of the pipelines, temperature in the transformers, etc. However, existing sensors employed in industry face challenges in terms of precision, rate, and consistency. Quantum sensors show great promise in this regard due to their ability to detect the smallest variations and can revolutionize the oil and gas industry.

It may be mentioned that superconducting quantum interference devices have shown potential for detecting magnetic fields. For instance, Bal et al.[143] have fabricated

https://doi.org/10.1021/acsomega.4c04406
ACS Omega 2025, 10, 2372−2392

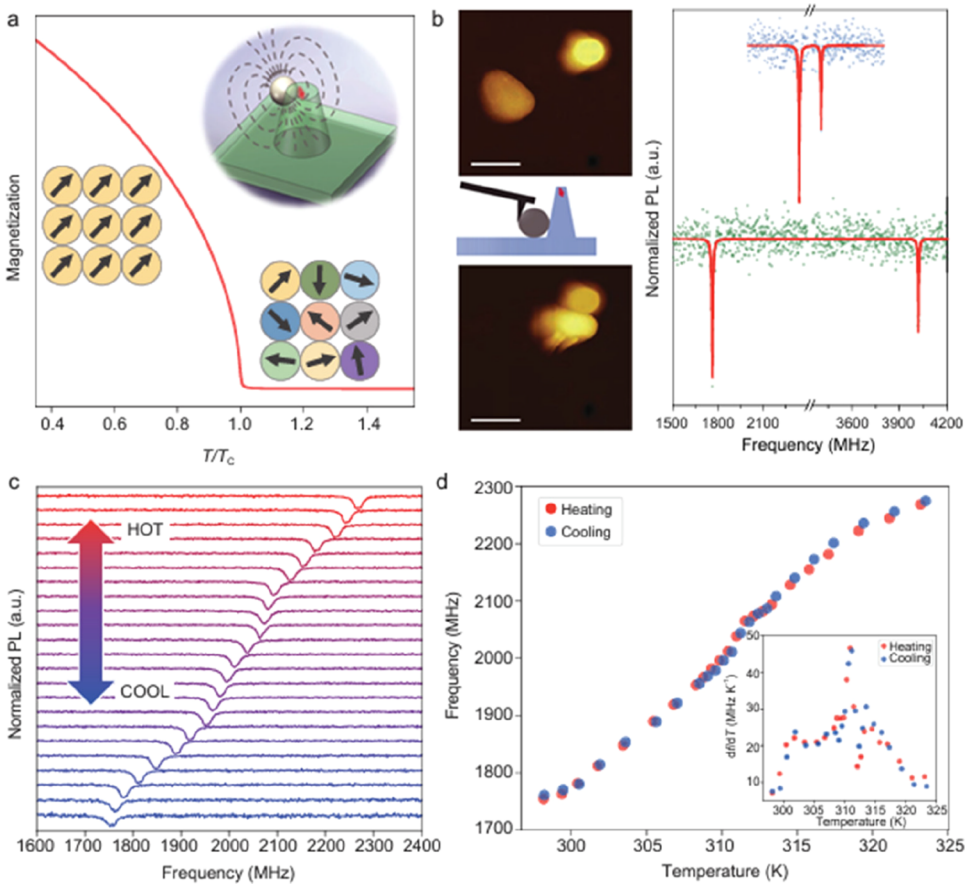

Figure 14. Design of a hybrid nanothermometer composed of a single magnetic copper−nickel alloy nanoparticle and a single nitrogen-vacancy (NV) center in a diamond nanopillar. (a) Simulation of the magnetization M of a copper−nickel alloy nanoparticle as a function of temperature under a magnetic field of 100 G. The inset illustrates the configuration of the hybrid nanothermometer. (b) Atomic force microscopy (AFM) image of the copper−nickel alloy magnetic nanoparticle (MNP) and the diamond nanopillar before the nanomanipulation (upper graph) and after the nanomanipulation (lower graph) and the corresponding optically detected magnetic resonance (ODMR) spectra of the single NV center before and after nanomanipulation (dots being measurement data and lines the double Lorentzian peak fitting). Scale bar is 1 μm. (c) ODMR spectra of the hybrid nanothermometer at different environmental temperatures (from 298 to 324 K from bottom to top). (d) ODMR frequency shifts in the heating (red) and cooling (blue) processes. The inset shows the temperature susceptibility of the hybrid nanothermometer, which has the maximum $df/dT \approx 47$ MHz K^{-1} (at 311 K).[149] Permission under the terms of the Creative Commons Attribution 4.0 International license.

sensors that can detect a magnetic field on the order of pT. However, they are normally expensive and lack dynamic range. Thus, diamond quantum sensors can be an alternative as they do not have the temperature constraint and have a better dynamical range. Ultrahigh sensitivity vector magnetometers can be fabricated using quantum diamonds, which can be used for pipeline monitoring. For instance, highly sensitive diamond quantum magnetometers can be used to detect the change in the magnetic field due to certain variation in the flow of oil/gas inside the pipeline, which can raise an alert about a potential leakage in the pipelines.

Quantum sensing has made an important contribution in the oil and gas industry. In the fossil fuel industry, quantum sensors can precisely map resources underground for discovery and recovery, this means scrupulously locating oil and gas reservoirs buried deep underground.[144] Compared to traditional exploration methods, quantum magnetometers and gravimeters are used to detect magnetic variations underground, by means of identifying resources underground.[145] Also, detailed maps of resources distributions are possible by deploying quantum sensors.[146]

Discovering a reservoir, a crucial challenge is to monitor it, which means tracking changes in pressure, temperature, and fluid flow. Not only in reservoir monitoring but also in refineries and long-distance transportation systems, a rise in temperature and pressure and potential leakage can damage the system. Quantum sensors, withstanding all challenges and extreme conditions, can precisely monitor and maintain these parameters, ensuring the integrity of the system and also minimizing environmental impacts.

While NV centers and SQUIDs both can detect magnetic fields at high precession, an advantage of using an NV center is that it can be used to measure the temperature also. As reported in 2010,[100] the zero-field splitting changes with temperature (in the 280−330 K range) with a coefficient of around −74 kHz/K. Temperature sensors are crucial for the oil and gas industry because they ensure that everything is working properly, providing safety measures in reservoir monitoring, refineries, and transportation systems.

Recent experimental work has demonstrated the capabilities of using NV diamond sensors for measuring various quantities. For instance, Toyli et al. have achieved 10 mK Hz$^{-1/2}$ sensitivity by monitoring the spin-dependent photoluminescence from NV centers in diamond.[147] By using dynamical coupling schemes, the spin coherence times have been enhanced by 45-fold indicating that these sensors can be

https://doi.org/10.1021/acsomega.4c04406
ACS Omega 2025, 10, 2372−2392

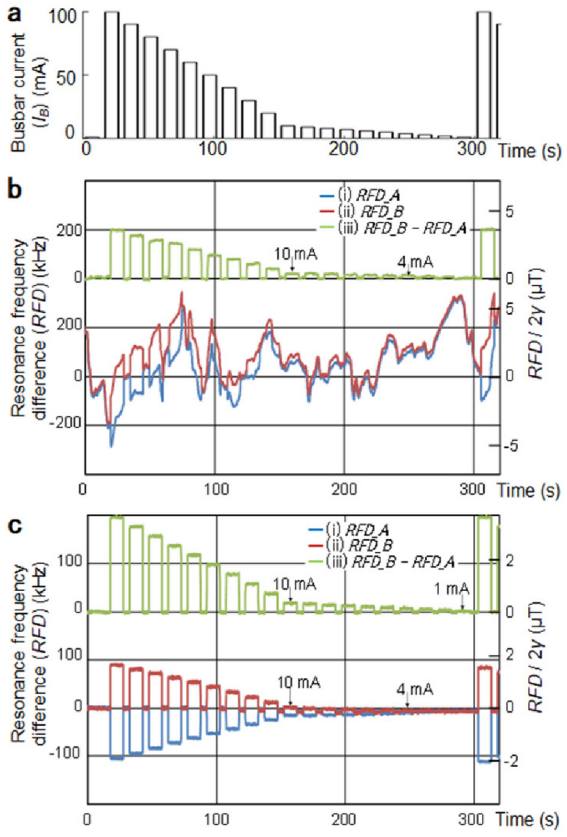

Figure 15. Determination of small current provided by reference source, a) current pulses supplied to busbar, 100 mA − 1 mA, b) resonance frequency difference (RFD) measurement from two sensors during daytime in a noisy environment, c) improved RFD measurement during midnight achieving around 1 mA accuracy [reprinted from ref 157 under a Creative Commons Attribution 4.0 International License].

leveraged for measuring local temperature with great precision. In another note, Wang et al. have demonstrated (Figure 13) sensitivity of a hybrid nanothermometer consisting of Cu-based nanoparticles and nanodiamond, which has shown sensitivity of 11 mK/$\sqrt{\text{Hz}}$ under ambient conditions.[148]

The measurement scheme has been improved further by Liu et al. achieving a sensitivity as high as 76 μK/$\sqrt{\text{Hz}}$ by using nanopillar arrays with NV centers (Figure 14).[148]

One of the drawbacks in the NV-based thermometry is the requirement of microwave excitation. This may lead to unwanted heating, which might be detrimental for the sample. To overcome this drawback, the silicon-vacancy (SiV) and germanium-vacancy (GeV) color centers in diamonds have recently been explored and have shown good optical temperature sensitivity owing to the temperature dependent wavelength optical zero-phonon line.[150] For instance, Choi et al. have used SiV in nanodiamonds to achieve an intrinsic noise floor of 13 mK $\text{Hz}^{-1/2}$.[151] On the other hand, Fan et al. have employed a GeV-based sensor demonstrating a resolution below 0.1 K in a wide range of temperatures.[152] Recently, Alkahtani et al. have reported tin-vacancy (SnV) color center in diamond-based thermometry with a sensitivity better than 0.2 K in 10 s integration time.[150] In addition, diamond-based sensors are inert under chemical treatment, can be used under high pressure conditions, and can work at high temperatures (>250 °C). Thus, color centers in diamond may serve as the best platform highly efficient thermometers for oil and gas industry which demand cost-effective robust thermometers for various applications like monitoring temperature in transformer/power grids, maintaining safety during coal mining, monitoring temperature in oil refineries, integrity of gas pipelines, etc.

7.1.1. Magnetic Anomaly Detection for Oil and Gas Exploration. There are other sensitive magnetometers with higher sensitivities that are being used for magnetic field detection. For instance, SQUID magnetometers are capable of detecting magnetic fields below 0.1 pT. However, they cannot be used for vector field measurement. In addition, the requirement of cryogenic temperatures makes the equipment complicated to operate. On the other hand, fluxgate magnetometers are limited by the noise generated by the thermal conductor (1 nT). Hall effect sensors suffer from poor resolution (0.1 μT). Thus, quantum diamond magnetometers can be a good alternative to the aforementioned sensors. The optically addressable spin states can easily be used to detect the magnetic field under ambient conditions.

It may be noted that detection of the magnetic anomalies in Earth's magnetic fields needs a calibrated magnetometer by sensing the permanent and induced magnetic field generated by the vessel. Without this knowledge, it is extremely difficult to detect crustal anomalies, which are extremely important to oil and gas exploration. Recently, Frontera et al. have used quantum diamond vector magnetometers for shipboard calibration purposes.[153] In another note, attempts have been made by Fleig and Frontera to map maritime magnetic anomalies.[153,154] These works demonstrate the potential of a quantum diamond magnetometer for oil and gas exploration and the possibility of employing these magnetometers for navigation purposes in the absence of a GPS signal.

7.2. Battery Research. Today's transport industry is making a transition from adopting fossil fuels to batteries in electric vehicles (EVs). This must be supported in-operando by accurate monitoring of the state of charge (SOC) of the battery which provides information about battery efficiency and other related parameters.[155] Thus, it is exigent to have access to an accurate sensor that can sense the currents with a high dynamic range (from 10 to 100 A).[156] On the contrary, typical accuracy of commercially existing devices is about 1 A. Hence, in this regard, diamond-based quantum sensors can play a major role by offering a better dynamical range.

One of the advantages of NV sensors is that they can also be used to measure the current of batteries very precisely in EV automobiles. In current EV automotives, the busbar technology is used instead of using cylindrical conductors, where the power is transmitted with thick rectangular shape conductors which are space efficient, good for high voltage application, and better in heat dissipation compared to cylindrical wires. As the current passes through the busbar, it generates a magnetic field outside the busbar. If the current passing through the bus bar changes, the magnetic field outside the bus bar also changes. The NV sensor, placed outside the busbar, is used to precisely measure this magnetic field, which basically provides accurate information about the current inside the busbar.

In general, a standard 4-wheeler EV can take around 130 A current, while on average it comes around 15 A. In terms of current sensors, their precise detection becomes crucial, specifically in noisy automobile environments. As discussed by Hatano et al.,[157] a "Busbar Current Differential Detection System" is developed, where two sensors, placed at two sides of

https://doi.org/10.1021/acsomega.4c04406
ACS Omega 2025, 10, 2372−2392

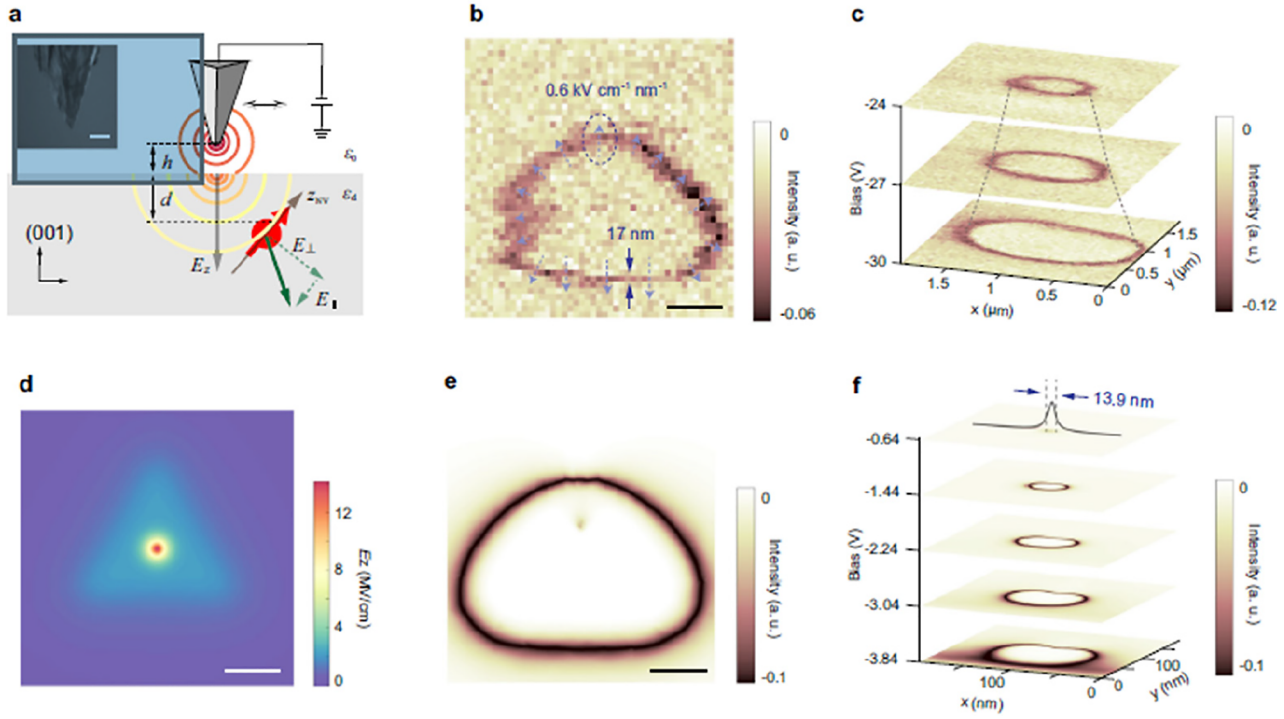

Figure 16. NV-based nanoscale scanning electrometry and quantitative estimation. (a) Schematic graph showing the simple triangular-tip model with a spherical tip apex. $E_\perp$ and $E_\parallel$ (green lines) are projected onto a NV with a depth of d at a tip height of h. During the simulation, we set ε_d = 5.7 for the diamond material. Inset: Scanning electron microscope (SEM) image of FIB-treated tungsten tip. Scale bar: 1 μm. (b) Scanning field-gradient imaging obtained at −16 V with an ODMR set point of 700 kHz. The dashed arrows reflect the direction and magnitude of field gradient. (c) Scanning field-gradient imaging of the tip under different biases. AFM set point: Δf_{AFM} = +10 Hz. Pulsed-ODMR set point: Δf = 400 kHz. (d) Simulated field distribution along the surface normal (E_z) from the triangular-tip model (a) with a side length of 220 nm, apex radius of 30 nm, h = 1 nm, d = 5 nm, and bias = −150 V. A field strength as large as 14.1 MV cm^{-1} can be experienced by the NV. (e) Simulated scanning-field gradient image at the bias = −10 V. The ODMR set point is set to be 700 kHz. The nonspherical shape arises from both the triangular tip and the fact that NV axis is not perpendicular to diamond surface. Scale bars in b, d, and e are 100 nm. (f) A series of simulated scanning gradient-field images under the same geometric parameters as in (e), demonstrating a precision of 13.9 nm for positioning the NV underneath.[160] Permission under the terms of the Creative Commons Attribution 4.0 International license.

a busbar, measure the magnetic field. In this way, the accuracy of 10 mA was achieved with a maximum current measured up to 130 A. With analog and digital control of the microwave frequency, a large current measurement system is also reported in a noisy environment.

For instance, batteries suffer from the problem of formation of solid-electrolyte interfaces or lithium plating that deteriorates the lifetime of the battery.[156,158] Thus, to monitor the changes in the electrolyte at the molecular level, one needs an *in situ* sensor with high spatial and temporal resolution.[158] As discussed earlier, the NV center in diamond is capable of measuring dc and ac electric fields and magnetic fields with great precision and sensitivity.[122,159] Measurement of the electric field distribution in electrolytes during battery operation can be the key to enhancing battery performance. Recently, Bian et al. have employed individual shallow NVs in diamond to quantitatively image electric field contours from a sharp tip of a qPlus-based atomic force microscope (Figure 16). They have achieved a spatial resolution of ∼10 nm.[160] This scanning electrometry work opens a new area for applying single quantum sensor for mapping charge and polarization of electric field at nanoscale resolution. In this work, NV centers were created by ion implantation close to the surface region (5−10 nm depth). Conductive AFM probes were brought to a specific fluorescence spot, and by using a qPlus sensor in frequency modulation mode, the authors could extract the electric field gradients with high spatial resolution.[160]

On another note, Hollendonner et al. have shown that nanodiamonds with NV centers work as in situ electric field sensors inside liquid electrolytes. They have demonstrated methodology for both static and moving nanodiamond sensor inside the electrolyte.[161]

Zhang et al. have performed nondestructive tests on small solid-state batteries by employing a microwave-free alternating current magnetometry technique.[162] Negatively charged NV centers in diamond having a specific cross-relaxation characteristic between NV centers and individual substitutional nitrogen centers occurring at 51.2 mT have been utilized to detect the eddy-current induced magnetic field of the battery.[162]

In order to enhance the cruising mileage and extend the lifetime of batteries, recently, Kubota et al. have fabricated a NV diamond sensor which can be used in electric vehicles (EVs) of dimension 1 × 1 × 0.5 cm^3 containing a high-pressure and high-temperature (HPHT) synthesized diamond with NV centers and multimode fiber.[163] The quantum sensor has demonstrated a current resolution of 10 mA over −150 to 150 °C temperature range with a bandwidth of 500 Hz under ambient conditions.

7.3. Photovoltaics. Today's green energy sector is largely dependent on the photovoltaic (PV) technology which requires sophisticated characterization techniques to explore

https://doi.org/10.1021/acsomega.4c04406
ACS Omega 2025, 10, 2372−2392

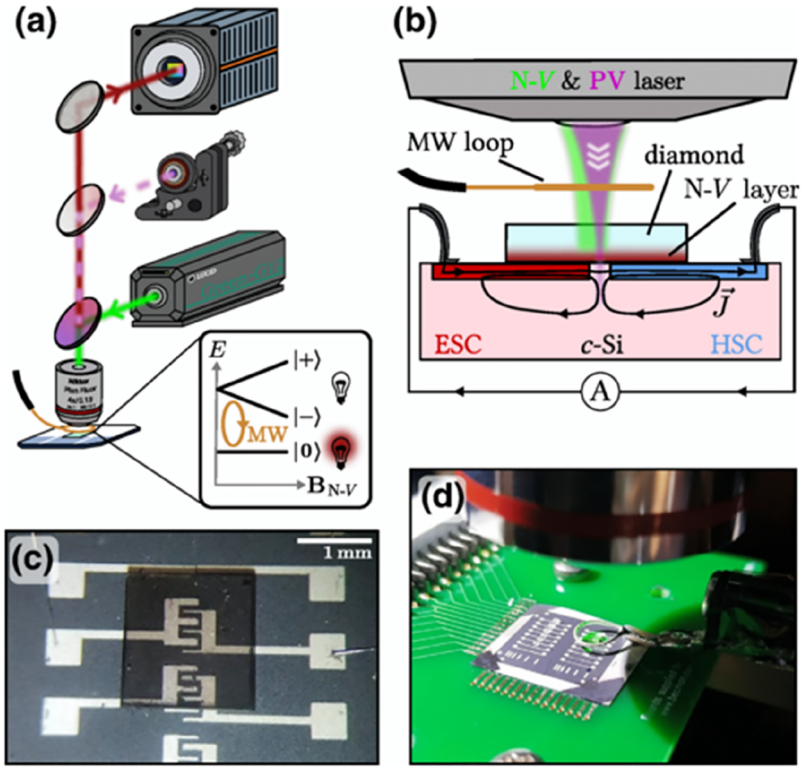

Figure 17. Imaging PV cells with a quantum diamond microscope. (a) Schematic of the experiment. A diamond containing a thin N−V layer is placed on top of the PV cell. The PV cell is stimulated with an infrared laser (pink dashed beam), while the N-Vs are controlled with a green laser (green beam). The N-Vs are readout via their photoluminescence (red beam) onto a camera. Magnetic imaging is achieved through measurement of the N−V's magnetic resonance in a process termed optically detected magnetic resonance (ODMR; inset). (b) Measurement geometry. The PV laser excites a current in the device (black arrows), which produces a magnetic field that is measured by the proximal N−V layer. Excited charges are collected selectively at the hole/electron selective contacts (H/ESC). (c) Photograph of diamond sensing chip on top of custom silicon PV device. (d) Wider view of sensing geometry, showing the microwave (MW) loop. Adapted with permission from ref 166. Copyright 2022 APS.

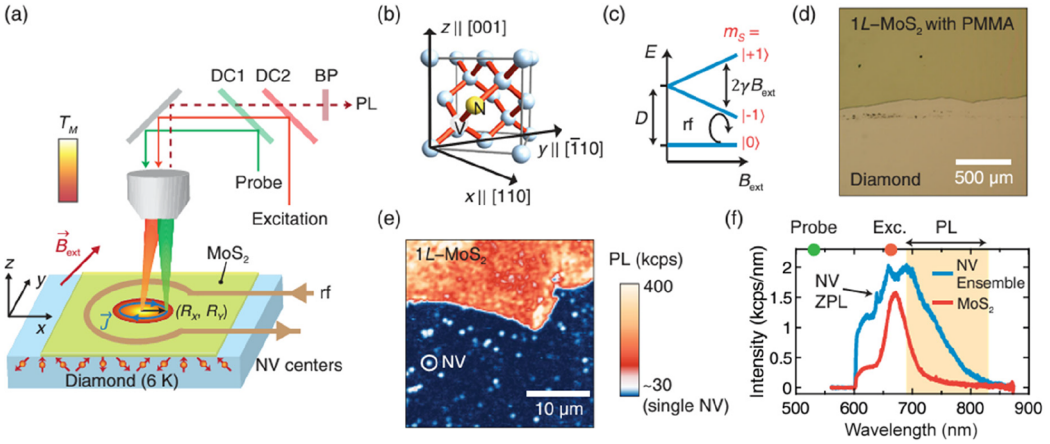

Figure 18. Mapping photocurrents inmonolayer MoS_2 with NV centers. (a) Experimental setup. A monolayer MoS_2 sheet is transferred onto a diamond sample hosting a near-surface ensemble of NV centers. An excitation laser (661 nm) generates a temperature distribution T_M within MoS_2 that drives a circulating photocurrent distribution J. The NV center senses the local magnetic field produced by the photocurrents and is optically readout by a separate probe laser (532 nm). DC1/DC2—dichroic mirrors at 550/685 nm; BP—bandpass (690−830 nm). (b) NV center in the diamond lattice. We address the subset of NV centers aligned with the [111] direction. (c) Energy levels of the NV spin triplet as a function of B_{ext}, the magnetic field parallel to the NV axis. Resonant microwave pulses (rf) manipulate an equal superposition of the m_s = |0> and |−1> states for phase acquisition. D—zero-field splitting. (d) Optical micrograph of monolayer MoS_2 on a diamond after vacuum transfer. To enhance optical contrast, this micrograph is taken prior to cleaning off a poly(methyl methacrylate) (PMMA) support layer. (e) Room-temperature PL image of the boundary between monolayer MoS_2 and bare diamond, containing single NV centers. (f) Room-temperature PL spectrum of monolayer MoS_2 and an ensemble NV sample under 532 nm illumination. The photoexcitation wavelength (661 nm) is longer than the NV zero-phonon line (ZPL; 637 nm) to minimize optical excitation of the NV center. The orange-shaded region depicts the collected PL for the NV spin readout. Adapted from ref 168. Published in 2020 by the American Physical Society under the terms of the Creative Commons Attribution 4.0 International license.

https://doi.org/10.1021/acsomega.4c04406
ACS Omega 2025, 10, 2372−2392

new materials and devices.[164] However, PV cells with higher efficiency suffer from carrier recombination issues and shunt resistances. These bottlenecks can be identified with a spatially resolved characterization technique apart from light beam induced current mapping (LBIC). Although LBIC is non-destructive, it needs a fully contacted device and lacks the quantitative information about localized carrier recombination.[165] In this regard, a quantum diamond microscope can play an important role in spatially identifying the defects in the PV module. For instance, Scholten et al. have employed a widefield nitrogen-vacancy microscope to monitor the currents induced by light in a silicon PV device (Figure 17).[166] The authors have achieved micrometer-scale resolution (identifying the internal current paths) of vector magnetic field imaging when the device has been illuminated with a focused laser beam. In addition, a time-resolved methodology has been implemented to image photocurrent build-up under illumination with microsecond resolution.[167]

In terms of imaging techniques, magnetic current imaging (MCI) using diamond quantum sensors has shown its potential in various applications. For instance, Nowodzinski et al. have described the use of a wide-field imaging technique using NV centers in diamond for current imaging at the redistributive layer level of integrated circuits. In addition, the implementation of vector magnetic field measurement for the MCI (with a reported resolution of 0.5 mA) calculation can be done at room temperature and atmospheric pressure.[167] This approach is quite relevant in studying packaging artifacts in solar cells.

As discussed earlier, accurate detection of photocurrent lies at the heart of optoelectronics devices and can be beneficial in understanding the light matter interaction. In this regard, a quantum diamond microscope can be unitized to image the photocurrent distribution within a material. For instance, Zhou et al. have developed a contact-free method detect photocurrent distributions quantum magnetometers for monolayer MoS_2.[168] In fact, by employing near surface NV centers in diamond, they have obtained a map of photothermal current distribution withing the 2-dimensional material. Their improvised technique successfully acquires a two-dimensional current density (having micron-sized photocurrent vortices) of 20 nA/μm with a projected sensitivity of 200 nA/($\mu m\sqrt{Hz}$) (Figure 18).[168] The spatiotemporal capabilities of the sensor have been further fortified by probing the rise time of the photocurrent.[168]

8. CONCLUSIONS

The influence of energy sectors in today's society spreads over all spheres including research and development, invention, manufacturing, transportability, and data processing. The need for developing green or renewable energy sources to mitigate pollution related issues is now at the forefront of research topics. In this work, we have discussed the relevance of quantum sensors in light of energy-related applications. Among various sensors, color centers in diamond are extremely important due to the presence of an optically addressable spin state and the possibility of room temperature operation. As an example, we briefly highlighted the methodology of magnetic field sensing using NV centers in diamond. We have identified three sectors, viz. (i) oil and gas industry, (ii) battery research, and (iii) photovoltaics related to energy applications where the quantum diamond sensors have practical advantages over existing sensors. The precision measurements with these sensors can be employed to detect leaks in oil and gas pipelines. Nanodiamond based thermometry can be used as new tools for monitoring temperature in the power supply units or battery temperature in electric vehicles. In addition, quantum diamond sensors can also be utilized to enhance the efficiency of photovoltaic cells by identifying current paths with high spatial resolution. Since their inception, quantum diamond sensors have not been free of challenges. For instance, mass production of various types of diamond is still lacking, which makes the quantum material quite expensive. Efficient conversion of NV centers after incorporating nitrogen into diamond is a topic of further research. In addition, efforts are required toward more industry-academia collaboration to deploy the product from laboratory testbed to real-world scenarios. Development of new protocols for improving the sensitivity of diamond-based quantum sensors is ongoing, and field deployable, cost-effective, commercial sensors can be anticipated in the near future.

AUTHOR INFORMATION

Corresponding Author

Tanmoy Basu − *Centre for Quantum Engineering, Research and Education, TCG CREST, Kolkata 700091, India; Academy of Scientific and Innovative Research (AcSIR), Ghaziabad 201002, India;* orcid.org/0000-0002-2249-5775; Email: tanmoyphys@gmail.com

Authors

Anupam Patra − *Centre for Quantum Engineering, Research and Education, TCG CREST, Kolkata 700091, India; Academy of Scientific and Innovative Research (AcSIR), Ghaziabad 201002, India*

Midhun Murali − *Centre for Quantum Engineering, Research and Education, TCG CREST, Kolkata 700091, India*

Mahesh Saini − *SUNAG Laboratory, Institute of Physics, Bhubaneswar 751005 Odisha, India; Homi Bhabha National Institute, Training School Complex, Mumbai 400085, India*

Amit Banerjee − *Microsystem Design-Integration Lab, Physics Department, Bidhan Chandra College, Asansol, West Bengal 713303, India*

Tapobrata Som − *SUNAG Laboratory, Institute of Physics, Bhubaneswar 751005 Odisha, India; Homi Bhabha National Institute, Training School Complex, Mumbai 400085, India*

Complete contact information is available at: https://pubs.acs.org/10.1021/acsomega.4c04406

Notes

The authors declare no competing financial interest.

ACKNOWLEDGMENTS

The authors would like thank Dr. Sachidananda Rath, IIT Bhubaneswar for his help with the Raman spectroscopy measurements. This work is partially supported by DST/TDT/DDP-38/2021, Device Development Programme (DDP), by the Department of Science & Technology (DST), Ministry of Science and Technology, Government of India. This work was performed with support from TCG CREST, Kolkata.

https://doi.org/10.1021/acsomega.4c04406
ACS Omega 2025, 10, 2372−2392

REFERENCES

(1) Degen, C. L.; Reinhard, F.; Cappellaro, P. Quantum Sensing. *Rev. Mod. Phys.* **2017**, *89* (3), No. 035002.

(2) Harris, I.; Ciccarino, C. J.; Flick, J.; Englund, D. R.; Narang, P. Group-III quantum defects in diamond are stable spin-1 color centers. *Phys. Rev. B* **2020**, *102* (19), No. 195206.

(3) Abend, S.; Allard, B.; Arnold, A. S.; Ban, T.; Barry, L.; Battelier, B.; Bawamia, A.; Beaufils, Q.; Bernon, S.; Bertoldi, A.; Bonnin, A.; Bouyer, P.; Bresson, A.; Burrow, O. S.; Canuel, B.; Desruelle, B.; Drougakis, G.; Forsberg, R.; Gaaloul, N.; Gauguet, A.; Gersemann, M.; Griffin, P. F.; Heine, H.; Henderson, V. A.; Herr, W.; Kanthak, S.; Krutzik, M.; Lachmann, M. D.; Lammegger, R.; Magnes, W.; Mileti, G.; Mitchell, M. W.; Mottini, S.; Papazoglou, D.; Pereira dos Santos, F.; Peters, A.; Rasel, E.; Riis, E.; Schubert, C.; Seidel, S. T.; Tino, G. M.; Van Den Bossche, M.; von Klitzing, W.; Wicht, A.; Witkowski, M.; Zahzam, N.; Zawada, M. Technology roadmap for cold-atoms-based quantum inertial sensor in space. AVS Quantum. *Science* **2023**, *5* (1), No. 019201.

(4) Wolf, F.; Schmidt, P. O. Quantum Sensing of Oscillating Electric Fields with Trapped Ions. *Measurement: Sensors* **2021**, *18*, No. 100271.

(5) Wolski, S. P.; Lachance-Quirion, D.; Tabuchi, Y.; Kono, S.; Noguchi, A.; Usami, K.; Nakamura, Y. Dissipation-Based Quantum Sensing of Magnons with a Superconducting Qubit. *Phys. Rev. Lett.* **2020**, *125* (11), No. 117701.

(6) Pirandola, S.; Bardhan, B. R.; Gehring, T.; et al. Advances in photonic quantum sensing. *Nature Photon* **2018**, *12*, 724−733.

(7) Bilmes, A.; Volosheniuk, S.; Brehm, J. D.; et al. Quantum sensors for microscopic tunneling systems. *npj Quantum Inf* **2021**, *7*, 27.

(8) Vettoliere, A.; Granata, C. Highly Sensitive Tunable Magnetometer Based on Superconducting Quantum Interference Device. *Sensors* **2023**, *23* (7), 3558.

(9) Facon, A.; Dietsche, E. K.; Grosso, D.; et al. A Sensitive Electrometer Based on a Rydberg Atom in a Schrödinger-cat State. *Nature* **2016**, *535*, 262−265.

(10) Fujiwara, M.; Shikano, Y. Diamond Quantum Thermometry: From Foundations to Applications. *Nanotechnology* **2021**, *32* (48), 482002.

(11) Stray, B.; Lamb, A.; Kaushik, A.; et al. Quantum Sensing for Gravity Cartography. *Nature* **2022**, *602*, 590−594.

(12) Bakhshandeh, S. Quantum Sensing Goes Bio. *Nat. Rev. Mater.* **2022**, *7*, 254.

(13) Pezzagna, S.; Meijer, J. Quantum Computer Based on Color Centers in Diamond. *Appl. Phys. Rev.* **2021**, *8* (1), No. 011308.

(14) Guo, X.; Stramma, A. M.; Li, Z.; Roth, W. G.; Huang, B.; Jin, Y.; Parker, R. A.; Martínez, J. A.; Shofer, N.; Michaels, C. P.; Purser, C. P.; Appel, M. H.; Alexeev, E. M.; Liu, T.; Ferrari, A. C.; Awschalom, D. D.; Delegan, N.; Pingault, B.; Galli, G.; Heremans, F. J.; Atatüre, M.; High, A. A. Microwave-Based Quantum Control and Coherence Protection of Tin-Vacancy Spin Qubits in a Strain-Tuned Diamond-Membrane Heterostructure. *Phys. Rev. X* **2023**, *13*, No. 041037.

(15) Bao, B.; Hua, Y.; Wang, R.; Li, D. Quantum-Based Magnetic Field Sensors for Biosensing. *Adv. Quantum Technol.* **2023**, *6*, No. 2200146.

(16) Bourgeois, E.; Gulka, M.; Nesladek, M. Photoelectric Detection and Quantum Readout of Nitrogen-Vacancy Center Spin States in Diamond. *Adv. Optical Mater.* **2020**, *8*, No. 1902132.

(17) Hayashi, K.; Matsuzaki, Y.; Taniguchi, T.; Shimo-Oka, T.; Nakamura, I.; Onoda, S.; Ohshima, T.; Morishita, H.; Fujiwara, M.; Saito, S.; Mizuochi, N. Optimization of Temperature Sensitivity Using the Optically Detected Magnetic-Resonance Spectrum of a Nitrogen-Vacancy Center Ensemble. *Phys. Rev. Appl.* **2018**, *10* (3), No. 034009.

(18) Ivády, V.; Simon, T.; Maze, J. R.; Abrikosov, I. A.; Gali, A. Pressure and temperature dependence of the zero-field splitting in the ground state of NV centers in diamond: A first-principles study. *Phys. Rev. B* **2014**, *90* (23), No. 235205.

(19) Fujisaku, T.; Tanabe, R.; Onoda, S.; Kubota, R.; Segawa, T. F.; So, F. T.-K.; Ohshima, T.; Hamachi, I.; Shirakawa, M.; Igarashi, R. pH Nanosensor Using Electronic Spins in Diamond. *ACS Nano* **2019**, *13* (10), 11726−11732.

(20) Laraoui, A.; Aycock-Rizzo, H.; Gao, Y.; et al. Imaging thermal conductivity with nanoscale resolution using a scanning spin probe. *Nat. Commun.* **2015**, *6*, 8954.

(21) Luo, T.; Lindner, L.; Langer, J.; Cimalla, V.; Vidal, X.; Hahl, F.; Schreyvogel, C.; Onoda, S.; Ishii, S.; Ohshima, T.; Wang, D.; Simpson, D. A.; Johnson, B. C.; Capelli, M.; Blinder, R.; Jeske, J. Creation of nitrogen-vacancy centers in chemical vapor deposition diamond for sensing applications. *New J. Phys.* **2022**, *24*, No. 033030.

(22) van Dam, S. B.; Walsh, M.; Degen, M. J.; Bersin, E.; Mouradian, S. L.; Galiullin, A.; Ruf, M.; IJspeert, M.; Taminiau, T. H.; Hanson, R.; Englund, D. R. Optical coherence of diamond nitrogen-vacancy centers formed by ion implantation and annealing. *Phys. Rev. B* **2019**, *99* (16), No. 161203.

(23) Lagomarsino, S.; Flatae, A. M.; Kambalathmana, H.; Sledz, F.; Hunold, L.; Soltani, N.; Reuschel, P.; Sciortino, S.; Gelli, N.; Massi, M.; Czelusniak, C.; Giuntini, L.; Agio, M. Creation of Silicon-Vacancy Color Centers in Diamond by Ion Implantation. *Front. Phys.* **2021**, *8*, No. 601362.

(24) Debroux, R.; Michaels, C. P.; Purser, C. M.; Wan, N.; Trusheim, M. E.; Arjona Martínez, J.; Parker, R. A.; Stramma, A. M.; Chen, K. C.; de Santis, L.; Alexeev, E. M.; Ferrari, A. C.; Englund, D.; Gangloff, D. A.; Atatüre, M. Quantum Control of the Tin-Vacancy Spin Qubit in Diamond. *Phys. Rev. X* **2021**, *11* (4), No. 041041.

(25) Ekimov, E. A.; Kondrin, M. V. Vacancy−impurity centers in diamond: prospects for synthesis and applications. *Physics-Uspekhi* **2017**, *60*, 539.

(26) Davis, G. Chapter 1. In *CVD Diamond for Electronic Devices and Sensors*; Sussmann, R. S., Ed.; Wiley, 2009.

(27) Collins, A. T. The detection of colour-enhanced and synthetic gem diamonds by optical spectroscopy. *Diamond Relat. Mater.* **2003**, *12* (10−11), 1976−1983.

(28) Henini, M. Properties and Growth of Diamond. In *Diamond*; Davies, G., Ed.; INSPEC, Institution of Electrical Engineers: London, UK, 1994; ISBN 0-85296-875-2.

(29) Xie, S.-Y.; Liu, F. The Structures, Synthesis, Properties, and Applications of Diamond. In *Functional Carbon Materials*; IOP Publishing Ltd, 2022; pp 7-1−7-27.

(30) Kaiser, W.; Bond, W. L. Nitrogen, A Major Impurity in Common Type I Diamond. *Phys. Rev.* **1959**, *115* (4), 857−863.

(31) Mainwood, A. Point Defects in Natural and Synthetic Diamond: What They Can Tell Us about CVD Diamond. *Phys. Status Solidi* **1999**, *172* (a), 25−35.

(32) Custers, J. F. H. Unusual Phosphorescence of a Diamond. *Physica* **1952**, *18* (8−9), 489−496.

(33) Rathnakara, V. K. K. Quantum Sensing with NV Centres in Diamond. Doctoral Thesis, Göttingen University, 2019.

(34) Fu, K.-M.; Santori, C.; Barclay, P.; Faraon, A.; Twitchen, D.; Markham, M.; Beausoleil, R. Properties of Implanted and CVD Incorporated Nitrogen-Vacancy Centers: Preferential Charge State and Preferential Orientation. In *Proceedings of SPIE - The International Society for Optical Engineering* **2011**, *7948*. DOI: 10.1117/12.876169.

(35) Lee, M. et al. Atomic Scale Magnetic Sensing and Imaging Based on Diamond NV Centers. In *Magnetometers - Fundamentals and Applications of Magnetism*; Intech Open, 2020. DOI: 10.5772/intechopen.84204.

(36) Childress, L.; Hanson, R. Diamond NV Centers for Quantum Computing and Quantum Networks. *MRS Bull.* **2013**, *38*, 134−138.

(37) Buchner, M.; Höfler, K.; Henne, B.; Ney, V.; Ney, A. Tutorial: Basic Principles, Limits of Detection, and Pitfalls of Highly Sensitive SQUID Magnetometry for Nanomagnetism and Spintronics. *J. Appl. Phys.* **2018**, *124* (16).

(38) Taylor, J.; Cappellaro, P.; Childress, L.; et al. High-sensitivity diamond magnetometer with nanoscale resolution. *Nat. Phys.* **2008**, *4*, 810−816.

(39) Schirhagl, R.; Chang, K.; Loretz, M.; Degen, C. L. Nitrogen-Vacancy Centers in Diamond: Nanoscale Sensors for Physics and Biology. *Annu. Rev. Phys. Chem.* **2014**, *65*, 83−105.

https://doi.org/10.1021/acsomega.4c04406
ACS Omega 2025, 10, 2372−2392

(40) Bragg, W. H.; Bragg, W. L. The structure of the diamond. *Proc. R. Soc. London A* **1913**, *89*, 277−29.
(41) Robertson, R.; Fox, J. J.; Martin, A. E. Two types of diamond. *Philos. Trans. R. Soc. London A* **1933**, *232*, 463−535.
(42) Aharonovich, I.; Neu, E. Diamond Nanophotonics. Adv. *Opt. Mater.* **2014**, *2*, 911−928.
(43) Zaitsev, A. M. *Optical Properties of Diamond, A Data Handbook*; Springer: Berlin, Heidelberg, 2001.
(44) McSkimin, H. J.; Andreatch, P. Elastic Moduli of Diamond as a Function of Pressure and Temperature. *J. Appl. Phys.* **1972**, *43* (7), 2944−2948.
(45) Bundy, F. P.; et al. Man-Made Diamonds. *Nature* **1955**, *176*, 51.
(46) Hall, H. T. Ultrahigh-Pressure Research. *Science* **1958**, *128* (3322), 445−449.
(47) Bundy, F. P. The P, T phase and reaction diagram for elemental carbon, 1979. *J. Geophys. Res. Solid Earth.* **1980**, *85* (B12), 6930−6936.
(48) Butler, J. E.; et al. Thin film diamond growth mechanisms. *Philos. Trans. A Math. Phys. Eng. Sci.* **1993**, *342* (1664), 209−224.
(49) Schwander, M.; Partes, K. A review of diamond synthesis by CVD processes. *Diam. Relat. Matter.* **2011**, *20* (9), 1287−1301.
(50) Vlasov, I. I.; Ralchenko, V. G.; Khomich, A. V.; Nistor, S. V.; Shoemaker, D.; Khmelnitskii, R. A. Relative Abundance of Single and Vacancy-Bonded Substitutional Nitrogen in CVD Diamond. *Phys. Stat. Sol. a* **2000**, *181*, 83.
(51) Mochalin, V. N.; et al. The Properties and Applications of Nanodiamonds. *Nat. Nanotechnol.* **2011**, *7*, 11 EP.
(52) Debuisschert, T. Quantum Sensing with Nitrogen-Vacancy Colour Centers in Diamond. *Photoniques* **2021**, *107*, 50−54.
(53) Shames, F. T.-K.; Terada, A. I.; Genjo, D.; Morishita, T.; Ohki, H.; Ohshima, I.; Onoda, S.; Takashima, H.; Takeuchi, S.; Mizuochi, N.; Igarashi, R.; Shirakawa, M.; Segawa, T. F. Anomalous Formation of Irradiation-Induced Nitrogen-Vacancy Centers in 5 nm-Sized Detonation Nanodiamonds. *J. Phys. Chem. C* **2022**, *126*, 5206−5217.
(54) Ishii, S.; Saiki, S.; Onoda, S.; Masuyama, Y.; Abe, H.; Ohshima, T. Ensemble Negatively-Charged Nitrogen-Vacancy Centers in Type-Ib Diamond Created by High Fluence Electron Beam Irradiation. *Quantum Beam Science* **2022**, *6*, 2.
(55) Crookes, W. *Diamonds*; Harper & Brothers: London, NY, 1909.
(56) Greentree, A. D.; Fairchild, B. A.; Hossain, F. M.; Prawer, S. Diamond Integrated Quantum Photonics. *Mater. Today* **2008**, *11*, 22.
(57) Fu, C. C.; Lee, H. Y.; Chen, K.; Lim, T. S.; Wu, H. Y.; Lin, P. K.; Wei, P. K.; Tsao, P. H.; Chang, H. C.; Fann, W. Characterization and Application of Single Fluorescent Nanodiamonds as Cellular Biomarkers. *Proc. Natl. Acad. Sci. U. S. A.* **2007**, *104*, 727.
(58) Jacques, V.; Wu, E.; Grosshans, F.; Treussart, F.; Grangier, P.; Aspect, A.; Roch, J. F. Experimental Realization of Wheeler's Delayed-Choice Gedanken Experiment. *Science* **2007**, *315*, 966−968.
(59) Childress, L.; Gurudev Dutt, M. V.; Taylor, J. M.; Zibrov, A. S.; Jelezko, F.; Wrachtrup, J.; Hemmer, P. R.; Lukin, M. D. Coherent Dynamics of Coupled Electron and Nuclear Spin Qubits in Diamond. *Science* **2006**, *314*, 281.
(60) Gurudev Dutt, M. V.; Childress, L.; Jiang, L.; Togan, E.; Maze, J.; Jelezko, F.; Zibrov, A. S.; Hemmer, P. R. Quantum Register Based on Individual Electronic and Nuclear Spin Qubits in Diamond. *Science* **2006**, *316*, 1312.
(61) Banerjee, A.; Das, D. Realizing a Variety of Carbon Nanostructures at Low Temperature using MW-PECVD of (CH_4 + H_2) Plasma. *Appl. Surf. Sci.* **2013**, *273*, 806−815.
(62) Banerjee, A.; Das, D. Low Temperature Synthesis of Spherical Nano-Diamond. *J. Exp. Nanosci.* **2014**, *9*, 818−824.
(63) Banerjee, A.; Das, D. Fabrication of Highly Transparent Diamond-like Carbon Anti-Reflecting Coating for Si Solar Cell Application. *AIP Conf. Proc.* **2014**, *1591*, 856−857.
(64) Das, D.; Banerjee, A. Anti-Reflection Coatings for Silicon Solar Cells from Hydrogenated Diamond-like Carbon. *Appl. Surf. Sci.* **2015**, *345*, 204−215.
(65) Das, D.; Banerjee, A. Further Improvements of Nano-Diamond Structures on Unheated Substrates by Optimization of Parameters with Secondary Plasma in MW-PECVD. *Surf. Coat. Technol.* **2015**, *272*, 357−365.
(66) Banerjee, A.; Das, D. Synthesis of Thin Film Nano-Diamonds on Unheated Substrates by Secondary Plasma in MW-PECVD. *AIP Conf. Proc.* **2015**, *1665*, No. 050077.
(67) Banerjee, A.; Das, D.; Sahoo, R. R. Anti-friction Diamond-like Carbon Nanocoatings for Advanced Tribological Applications. *American Institute of Physics Conf. Proc.* **1832**, *2017*, No. 080036.
(68) A Banerjee, A.; Das, D. Nano-Diamond and Diamond-Like Carbon Thin Films for Anti-Reflecting Coating Application on Silicon Solar Cells. *Materials Today: Proceedings* **2018**, *5*, 23316−23320.
(69) Agarwal, D.; Dole, N.; Banerjee, A.; Banerjee, A. Nano-diamonds for advanced photonic and biomedical applications in Carbon Quantum Dots for Sustainable Energy and Optoelectronics. In *Carbon Quantum Dots for Sustainable Energy and Optoelectronics*; Elsevier Publishing, 2023; pp 455−472.
(70) Ostrikov, K.; Cvelbar, U.; Murphy, A. B. Plasma nanoscience: setting directions, tackling grand challenges. *J. Phys. D: Appl. Phys.* **2011**, *44*, 174001.
(71) May, P. W. CVD diamond: a new technology for the future? *Endeavour* **1995**, *19*, 101.
(72) May, P. W. Diamond thin films: a 21st-century material. *Philos. Trans. of the Royal Soc. A* **2000**, *358*, 473.
(73) Asmussen, J.; Reinhard, D., Eds.; *Diamond Films Handbook*, first ed.; CRC Press, 2002.
(74) Asmann, M.; Heberlein, J.; Pfender, E. Experimental Confirmation of Thermal Plasma CVD of Diamond with Liquid Feedstock Injection Model. *Diamond Relat. Mater.* **1999**, *9* (1), 13−21.
(75) Chu, Y.C.; Jiang, G.; Chang, C.; Ting, J.M.; Lee, H.L.; Tzen, Y. *11th IEEE International Conference on Nanotechnology*; Oregon, USA, Portland, 2011; p 2011.
(76) Potocky, S.; Kromka, A.; Potmesil, J.; Remes, Z.; Vorlicek, V.; Vanecek, M.; Michalka, M. Investigation of nanocrystalline diamond films grown on silicon and glass at substrate temperature below 400 °C. *Diam. Rel. Mater.* **2007**, *16*, 744.
(77) Daenen, M.; Williams, O. A.; D'Haen, J.; Haenen, K.; Nesládek, M. Seeding, growth and characterization of nanocrystalline diamond films on various substrates. *Phys. Status Solidi* **2006**, *203* (a), 3005.
(78) Tsugawa, K.; Ishihara, M.; Kim, J.; Hasegawa, M.; Koga, Y. Large-Area and Low-Temperature Nanodiamond Coating by Microwave Plasma Chemical Vapor Deposition. *J. New Diam. Frontier Carb. Techn.* **2006**, *16*, 337.
(79) Kumar, S.; Rauthan, C. M. S.; Srivatsa, K. M. K.; Dixit, P. N.; Bhattacharyya, R. Realization of different carbon nanostructures by a microwave plasma enhanced chemical vapor deposition technique. *Appl. Surf. Sci.* **2001**, *182*, 326.
(80) López, J. M.; Gordillo-Vázquez, F. J.; Albella, J. M. Nanocrystalline diamond thin films deposited by 35 kHz Ar-rich plasmas. *Appl. Surf. Sci.* **2002**, *185*, 321.
(81) Hara, T.; Yoshitake, T.; Fukugawa, T.; Zhu, L. y.; Itakura, M.; Kuwano, N.; Nagayama, K. Nanocrystalline diamond film prepared by pulsed laser deposition in a hydrogen atmosphere. *Diamond Relat. Mater.* **2004**, *13* (4−8), 679−683.
(82) Plakhotnik, T.; Aman, H. NV-Centers in Nanodiamonds: How Good They Are. *Diamond Relat. Mater.* **2018**, *82*, 87−95.
(83) Mzyk, A.; Sigaeva, A.; Schirhagl, R. Relaxometry with Nitrogen Vacancy (NV) Centers in Diamond. *Acc. Chem. Res.* **2022** *55*(24), 3572−3580..
(84) Ficek, M.; Głowacki, M. J.; Gajewski, K.; Kunicki, P.; Gacka, E.; Sycz, K.; Mrózek, M.; Wojciechowski, A. M.; Gotszalk, T. P.; Gawlik, W.; et al. Integration of Fluorescent, NV-Rich Nanodiamond Particles with AFM Cantilevers by Focused Ion Beam for Hybrid Optical and Micromechanical Devices. *Coatings* **2021**, *11*, 1332.
(85) Xia, K.; Liu, C. F.; Leong, W. H.; et al. Nanometer-precision non-local deformation reconstruction using nanodiamond sensing. *Nat. Commun.* **2019**, *10*, 3259.

https://doi.org/10.1021/acsomega.4c04406
ACS Omega 2025, 10, 2372−2392

(86) Schell, A. W.; Kewes, G.; Schröder, T.; Wolters, J.; Aichele, T.; Benson, O. A scanning probe-based pick-and-place procedure for assembly of integrated quantum optical hybrid devices. *Rev. Sci. Instrum.* **2011**, *82* (7), No. 073709.
(87) Rondin, L.; Tetienne, J. P.; Rohart, S.; Thiaville, A.; Hingant, T.; Spinicelli, P.; et al. Stray-field imaging of magnetic vortices with a single diamond spin. *Nat. Commun.* **2013**, *4*, 1−5.
(88) Weber, J. R.; Koehl, W. F.; Varley, J. B.; Janotti, A.; Buckley, B. B.; Van de Walle, C. G.; Awschalom, D. D. Quantum Computing with Defects. *Proc. Natl. Acad. Sci. U.S.A.* **2010**, *107* (19), 8499−8518.
(89) Loubser, J. H. N.; van Wyk, J. A. Electron Spin Resonance in the Study of Diamond. *Rep. Prog. Phys.* **1978**, *41* (8), 1201.
(90) Liu, G. Q.; Feng, X.; Wang, N.; et al. Coherent Quantum Control of Nitrogen-Vacancy Center Spins near 1000 K. *Nat. Commun.* **2019**, *10*, 1344.
(91) Rogers, L. J.; Armstrong, S.; Sellars, M. J.; Manson, N. B. Infrared Emission of the NV Center in Diamond: Zeeman and Uniaxial Stress Studies. *New J. Phys.* **2008**, *10*, 103024.
(92) Rondin, L.; Tetienne, J.-P.; Hingant, T.; Roch, J.-F.; Maletinsky, P.; Jacques, V. Magnetometry with Nitrogen-Vacancy Defects in Diamond. *Rep. Prog. Phys.* **2014**, *77* (5), No. 056503.
(93) Segawa, T. F.; Igarashi, R. Nanoscale Quantum Sensing with Nitrogen-Vacancy Centers in Nanodiamonds − A Magnetic Resonance Perspective. *Prog. Nucl. Magn. Reson. Spectrosc.* **2023**, *134*−*135*, 20−38.
(94) Tetienne, J.-P.; Rondin, L.; Spinicelli, P.; Chipaux, M.; Debuisschert, T.; Roch, J.-F.; Jacques, V. Magnetic-Field-Dependent Photodynamics of Single NV Defects in Diamond: An Application to Qualitative All-Optical Magnetic Imaging. *New J. Phys.* **2012**, *14* (10), No. 103033.
(95) Stanwix, P. L.; Pham, L. M.; Maze, J. R.; Le Sage, D.; Yeung, T. K.; Cappellaro, P.; Hemmer, P. R.; Yacoby, A.; Lukin, M. D.; Walsworth, R. L. Coherence of Nitrogen-Vacancy Electronic Spin Ensembles in Diamond. *Phys. Rev. B* **2010**, *82* (20), No. 201201.
(96) Oort, E. v.; et al. Optically Detected Spin Coherence of the Diamond N-V Center in Its Triplet Ground State. *J. Phys. C: Solid State Phys.* **1988**, *21*, 4385−4391.
(97) Kittel, C. *Introduction to Solid State Physics*; 7th ed.; Wiley Pvt. Limited: New York, 2007.
(98) Tsunaki, L. B. E. Undergraduate Thesis: Quantum Information Processing with Nitrogen-Vacancy Centers in Diamonds. Sao Carlos Institute of Physics, University of Sao Paulo, **2020**.
(99) Weil, J. A.; Bolton, J. R. *Electron Paramagnetic Resonance: Elementary Theory and Practical Applications*; Wiley: 2007.
(100) Acosta, V. M.; et al. Temperature Dependence of the Nitrogen-Vacancy Magnetic Resonance in Diamond. *Phys. Rev. Lett.* **2010**, *104* (7), No. 070801.
(101) Jeong, K.; et al. Understanding the Magnetic Resonance Spectrum of Nitrogen-Vacancy Centers in an Ensemble of Randomly Oriented Nanodiamonds. *J. Phys. Chem. C* **2017**, *121* (38), 21057−21061.
(102) He, X. F.; Manson, N. B.; Fisk, P. T. Paramagnetic Resonance of Photoexcited N-V Defects in Diamond. II. Hyperfine Interaction with the N14 Nucleus. *Phys. Rev. B* **1993**, *47* (14), 8816−8822.
(103) Steiner, M.; Neumann, P.; Beck, J.; Jelezko, F.; Wrachtrup, J. Universal Enhancement of the Optical Readout Fidelity of Single Electron Spins at Nitrogen-Vacancy Centers in Diamond. *Phys. Rev. B* **2010**, *81* (3), No. 035205.
(104) Guo, S. An Overview of NV Centers. *J. Appl. Math. Phys.* **2023**, *11*, 3666−3675.
(105) Qnami, Qnami Technical Note: Fundamentals of Magnetic Field Measurement with NV Centers in Diamond, 2020.
(106) Breev, I. D.; Yakovleva, V. V.; Anisimov, A. N. NV-Center Distribution and ODMR Spectra in Two Types of Natural Diamonds. *J. Phys.: Conf. Ser.* **2022**, *2227*, No. 012031.
(107) Murzin, D.; Mapps, D. J.; Levada, K.; Belyaev, V.; Omelyanchik, A.; Panina, L.; Rodionova, V. Ultrasensitive Magnetic Field Sensors for Biomedical Applications. *Sensors* **2020**, *20* (6), 1569.
(108) Grosz, A.; Haji-Sheikh, M. J.; Mukhopadhyay, S. C., Eds. *High Sensitivity Magnetometers*; Springer: Switzerland, 2017.
(109) Yarar, E.; Salzer, S.; Hrkac, V.; Piorra, A.; Höft, M.; Knöchel, R.;··· Quandt, E. Inverse Bilayer Magnetoelectric Thin Film Sensor. *Appl. Phys. Lett.* **2016**, *109* (2).
(110) Wang, Y.; Gray, D.; Berry, D.; Gao, J.; Li, M.; Li, J.; Viehland, D. An Extremely Low Equivalent Magnetic Noise Magnetoelectric Sensor. *Adv. Mater.* **2011**, *23* (35), 4111.
(111) Vetoshko, P. M.; Gusev, N. A.; Chepurnova, D. A.; Samoilova, E. V.; Syvorotka, I. I.; Syvorotka, I. M.; Belotelov, V. I. Flux-Gate Magnetic Field Sensor Based on Yttrium Iron Garnet Films for Magnetocardiography Investigations. *Technol. Phys. Lett.* **2016**, *42*, 860−864.
(112) Murata, N.; Karo, H.; Sasada, I.; Shimizu, T. Fundamental Mode Orthogonal Fluxgate Magnetometer Applicable for Measurements of DC and Low-Frequency Magnetic Fields. *IEEE Sens. J.* **2018**, *18* (7), 2705−2712.
(113) Butta, M.; Janosek, M.; Schutte, B. P.; Vazquez, M.; Perez, R.; Ramirez, E. C.; Jimenez, A. Effect of Amorphous Wire Core Diameter on the Noise of an Orthogonal Fluxgate. *IEEE Trans. Magn.* **2018**, *54* (11), 1−5.
(114) Kirtley, J. R.; Ketchen, M. B.; Stawiasz, K. G.; Sun, J. Z.; Gallagher, W. J.; Blanton, S. H.; Wind, S. J. High-Resolution Scanning SQUID Microscope. *Appl. Phys. Lett.* **1995**, *66* (9), 1138−1140.
(115) Forstner, S.; Prams, S.; Knittel, J.; Van Ooijen, E. D.; Swaim, J. D.; Harris, G. I.; Rubinsztein-Dunlop, H. Cavity Optomechanical Magnetometer. *Phys. Rev. Lett.* **2012**, *108* (12), 120801.
(116) Li, B. B.; Bílek, J.; Hoff, U. B.; Madsen, L. S.; Forstner, S.; Prakash, V.; Andersen, U. L. Quantum Enhanced Optomechanical Magnetometry. *Optica* **2018**, *5* (7), 850−856.
(117) Li, B. B.; Bulla, D.; Prakash, V.; Forstner, S.; Dehghan-Manshadi, A.; Rubinsztein-Dunlop, H.; Bowen, W. P. Scalable High-Sensitivity Optomechanical Magnetometers on a Chip. *Apl Photonics* **2018**, *3* (12).
(118) Schulz, L.; Heinisch, P.; Richter, I. Calibration of Off-the-Shelf Anisotropic Magnetoresistance Magnetometers. *Sensors* **2019**, *19* (8), 1850.
(119) Rifai, D.; Abdalla, A. N.; Ali, K.; Razali, R. Giant Magnetoresistance Sensors: A Review on Structures and Non-Destructive Eddy Current Testing Applications. *Sensors* **2016**, *16* (3), 298.
(120) Reig, C.; Cardoso, S.; Mukhopadhyay, S. C. Giant Magnetoresistance (GMR) Sensors. *Smart Sensors, Measurement and Instrumentation* **2013**, *6* (1), 1−301.
(121) Li, J.; Liu, H.; Bi, T. Tunnel Magnetoresistance-Based Noncontact Current Sensing and Measurement Method. *IEEE Transactions on Instrumentation and Measurement* **2022**, *71*, 1−9.
(122) Wolf, T.; Neumann, P.; Nakamura, K.; Sumiya, H.; Ohshima, T.; Isoya, J.; Wrachtrup, J. Subpicotesla Diamond Magnetometry. *Phys. Rev. X* **2015**, *5* (4), No. 041001.
(123) Fescenko, I.; Jarmola, A.; Savukov, I.; Kehayias, P.; Smits, J.; Damron, J.; Ristoff, N.; Mosavian, N.; Acosta, V. M. Diamond magnetometer enhanced by ferrite flux concentrators. *Phys. Rev. Res.* **2020**, *2*, No. 023394.
(124) Zhang, C.; Shagieva, F.; Widmann, M.; Kübler, M.; Vorobyov, V.; Kapitanova, P.; Nenasheva, E.; Corkill, R.; Rhrle, O.; Nakamura, K.; Sumiya, H.; Onoda, S.; Isoya, J.; Wrachtrup, J. Diamond Magnetometry and Gradiometry Towards Subpicotesla dc Field Measurement. *Phys. Rev. Appl.* **2021**, *15* (6), No. 064075.
(125) Barry, J. F.; Schloss, J. M.; Bauch, E.; Turner, M. J.; Hart, C. A.; Pham, L. M.; Walsworth, R. L. Sensitivity Optimization for NV-Diamond Magnetometry. *Rev. Mod. Phys.* **2020**, *92* (1), No. 015004.
(126) Balasubramanian, G.; Neumann, P.; Twitchen, D.; Markham, M.; Kolesov, R.; Mizuochi, N.; Wrachtrup, J. Ultralong Spin Coherence Time in Isotopically Engineered Diamond. *Nat. Mater.* **2009**, *8* (5), 383−387.
(127) Boss, J. M.; Cujia, K. S.; Zopes, J.; Degen, C. L. Quantum Sensing with Arbitrary Frequency Resolution. *Science* **2017**, *356* (6340), 837−840.

https://doi.org/10.1021/acsomega.4c04406
ACS Omega 2025, 10, 2372−2392

(128) Hernández-Gómez, S.; Poggiali, F.; Cappellaro, P.; Fabbri, N. Noise Spectroscopy of a Quantum-Classical Environment with a Diamond Qubit. *Phys. Rev. B* **2018**, *98* (21), 214307.
(129) Knowles, H. S.; Kara, D. M.; Atatüre, M. Observing Bulk Diamond Spin Coherence in High-Purity Nanodiamonds. *Nat. Mater.* **2014**, *13* (1), 21−25.
(130) De Lange, G.; Van Der Sar, T.; Blok, M.; Wang, Z. H.; Dobrovitski, V.; Hanson, R. Controlling the Quantum Dynamics of a Mesoscopic Spin Bath in Diamond. *Sci. Rep.* **2012**, *2* (1), 382.
(131) Bauch, E.; Singh, S.; Lee, J.; Hart, C. A.; Schloss, J. M.; Turner, M. J.; Walsworth, R. L. Decoherence of Dipolar Spin Ensembles in Diamond. *arXiv preprint* **2019**, arXiv:1904.08763.
(132) Maze, J. R.; Stanwix, P. L.; Hodges, J. S.; Hong, S.; Taylor, J. M.; Cappellaro, P.; Jiang, L.; Gurudev Dutt, M. V.; Togan, E.; Zibrov, A. S.; Yacoby, A.; Walsworth, R. L.; Lukin, M. D. Nanoscale Magnetic Sensing with an Individual Electronic Spin in Diamond. *Nature* **2008**, *455* (7213), 644−647.
(133) Zhao, Z.; Ye, X.; Xu, S.; Yu, P.; Yang, Z.; Kong, X.; Wang, Y.; Xie, T.; Shi, F.; Du, J. Sub-Nanotesla Sensitivity at the Nanoscale with a Single Spin. *Natl. Sci. Rev.* **2023**, *10* (12), nwad100.
(134) Meirzada, I.; Hovav, Y.; Wolf, S. A.; Bar-Gill, N. Negative Charge Enhancement of Near-Surface Nitrogen Vacancy Centers by Multicolor Excitation. *Phys. Rev. B* **2018**, *98* (24), 245411.
(135) Wee, T. L.; Tzeng, Y. K.; Han, C. C.; Chang, H. C.; Fann, W.; Hsu, J. H.; Yu, Y. C. Two-Photon Excited Fluorescence of Nitrogen-Vacancy Centers in Proton-Irradiated Type Ib Diamond. *J. Phys. Chem. A* **2007**, *111* (38), 9379−9386.
(136) Clement, J. D. Magnetic Sensing with Large Ensembles of Nitrogen-Vacancy Centers in Diamond. *Department of Physics, Technical University of Denmark*, 2022; p 106.
(137) Scholten, S. C.; Healey, A. J.; Robertson, I. O.; Abrahams, G. J.; Broadway, D. A.; Tetienne, J. P. Widefield Quantum Microscopy with Nitrogen-Vacancy Centers in Diamond: Strengths, Limitations, and Prospects. *J. Appl. Phys.* **2021**, *130* (15).
(138) Parashar, M.; Bathla, A.; Shishir, D.; Gokhale, A.; Bandyopadhyay, S.; Saha, K. Sub-second Temporal Magnetic Field Microscopy Using Quantum Defects in Diamond. *Sci. Rep.* **2022**, *12* (1), 8743.
(139) Glenn, D. R.; Fu, R. R.; Kehayias, P.; Le Sage, D.; Lima, E. A.; Weiss, B. P.; Walsworth, R. L. Micrometer-scale Magnetic Imaging of Geological Samples Using a Quantum Diamond Microscope. *Geochem. Geophys. Geosyst.* **2017**, *18* (8), 3254−3267.
(140) Turner, M. J.; Langellier, N.; Bainbridge, R.; Walters, D.; Meesala, S.; Babinec, T. M.; Levine, E. V. Magnetic Field Fingerprinting of Integrated-Circuit Activity with a Quantum Diamond Microscope. *Phys. Rev. Appl.* **2020**, *14* (1), No. 014097.
(141) Appel, P. Scanning Nanomagnetometry: Probing Magnetism with Single Spins in Diamond, 2017.
(142) Rondin, L.; Tetienne, J. P.; Spinicelli, P.; Dal Savio, C.; Karrai, K.; Dantelle, G.; Jacques, V. Nanoscale Magnetic Field Mapping with a Single Spin Scanning Probe Magnetometer. *Appl. Phys. Lett.* **2012**, *100* (15).
(143) Bal, M.; Deng, C.; Orgiazzi, J. L.; et al. Ultrasensitive Magnetic Field Detection Using a Single Artificial Atom. *Nat. Commun.* **2012**, *3*, 1324.
(144) Crawford, S. E.; Shugayev, R. A.; Paudel, H. P.; Lu, P.; Syamlal, M.; Ohodnicki, P. R.; Chorpening, B.; Gentry, R.; Duan, Y. Quantum Sensing for Energy Applications: Review and Perspective. *Advanced Quantum Technologies* **2021**, *4*, 8. DOI: 10.1002/qute.202100049.
(145) Zhou, M.-K.; Duan, X.-C.; Chen, Le-Le; Luo, Q.; Xu, Y.-Y.; Hu, Z.-K. "Micro-Gal level gravity measurements with cold atom interferometry." *Chinese Physics B* **2015**, *24*, 5. DOI: 10.1088/1674-1056/24/5/050401.
(146) Balasubramanian, G.; Chan, I. Y.; Kolesov, R.; Al-Hmoud, M.; Tisler, J.; Shin, C.; Kim, C.; Wojcik, A.; Hemmer, P. R.; Krueger, A.; Hanke, T.; Leitenstorfer, A.; Bratschitsch, R.; Jelezko, F.; Wrachtrup, J. Nanoscale imaging magnetometry with diamond spins under ambient conditions. *Nature* **2008**, *455* (7213), 648−651.
(147) Toyli, D. M.; de las Casas, C. F.; Christle, D. J.; Dobrovitski, V. V.; Awschalom, D. D. Fluorescence Thermometry Enhanced by the Quantum Coherence of Single Spins in Diamond. *Proc. Natl. Acad. Sci. U.S.A.* **2013**, *110* (21), 8417−8421.
(148) Wang, N.; Liu, G.-Q.; Leong, W.-H.; Zeng, H.; Feng, X.; Li, S.-H.; Dolde, F.; Fedder, H.; Wrachtrup, J.; Cui, X.-D.; Yang, S.; Li, Q.; Liu, R.-B. Magnetic Criticality Enhanced Hybrid Nanodiamond Thermometer under Ambient Conditions. *Phys. Rev. X* **2018**, *8* (1), No. 011042.
(149) Liu, C.-F.; Leong, W.-H.; Xia, K.; Feng, X.; Finkler, A.; Denisenko, A.; Wrachtrup, J.; Li, Q.; Liu, R.-B. Ultra-Sensitive Hybrid Diamond Nanothermometer. *Natl. Sci. Rev.* **2021**, *8* (5), No. nwaa194.
(150) Alkahtani, M.; Cojocaru, I.; Liu, X.; Herzig, T.; Meijer, J.; Küpper, J.; Lühmann, T.; Akimov, A. V.; Hemmer, P. R. Tin-Vacancy in Diamonds for Luminescent Thermometry. *Appl. Phys. Lett.* **2018**, *112* (24), 241902.
(151) Choi, S.; Agafonov, V. N.; Davydov, V. A.; Plakhotnik, T. Ultrasensitive All-Optical Thermometry Using Nanodiamonds with a High Concentration of Silicon-Vacancy Centers and Multiparametric Data Analysis. *ACS Photonics* **2019**, *6* (6), 1387−1392.
(152) Fan, J.-W.; Cojocaru, I.; Becker, J.; Fedotov, I. V.; Alkahtani, M. H. A.; Alajlan, A.; Blakley, S.; Rezaee, M.; Lyamkina, A.; Palyanov, Y. N.; Borzdov, Y. M.; Yang, Y.-P.; Zheltikov, A.; Hemmer, P.; Akimov, A. V. Germanium-Vacancy Color Center in Diamond as a Temperature Sensor. *ACS Photonics* **2018**, *5* (3), 765−770.
(153) Frontera, P.; Alessandrini, S.; Stetson, J. Shipboard calibration of a diamond nitrogen vacancy magnetic field sensor. *2018 IEEE/ION Position, Location and Navigation Symposium (PLANS)* **2018**, DOI: 10.1109/plans.2018.8373418.
(154) Fleig, T.; Frontera, P. Maritime magnetic anomaly mapping with a diamond nitrogen vacancy sensor. *2018 IEEE/ION Position, Location and Navigation Symposium (PLANS)* **2018**, DOI: 10.1109/plans.2018.8373493.
(155) Kurzweil, P.; Scheuerpflug, W. State-of-Charge Monitoring and Battery Diagnosis of Different Lithium Ion Chemistries Using Impedance Spectroscopy. *Batteries* **2021**, *7*, 17.
(156) Szumska, E. M.; Jurecki, R. S. Parameters Influencing on Electric Vehicle Range. *Energies* **2021**, *14* (16), 4821.
(157) Hatano, Y.; Shin, J.; Tanigawa, J.; et al. High-precision robust monitoring of charge/discharge current over a wide dynamic range for electric vehicle batteries using diamond quantum sensors. *Sci. Rep* **2022**, *12*, 13991.
(158) Meda, U. S.; Lal, L.; Sushantha, M.; Garg, P. Solid Electrolyte Interphase (SEI), a Boon or a Bane for Lithium Batteries: A Review on the Recent Advances. *J. Energy Storage* **2022**, *47*, No. 103564.
(159) Dolde, F.; Fedder, H.; Doherty, M.; et al. Electric-Field Sensing Using Single Diamond Spins. *Nat. Phys.* **2011**, *7*, 459−463.
(160) Bian, K.; Zheng, W.; Zeng, X.; et al. Nanoscale Electric-Field Imaging Based on a Quantum Sensor and Its Charge-State Control under Ambient Condition. *Nat. Commun.* **2021**, *12*, 2457.
(161) Hollendonner, M.; Sharma, S.; Parthasarathy, S. K.; Dasari, D. B. R.; Finkler, A.; Kusminskiy, S. V.; Nagy, R. Quantum Sensing of Electric Field Distributions of Liquid Electrolytes with NV-Centers in Nanodiamonds. *New J. Phys.* **2023**, *25*, No. 093008.
(162) Zhang, X.; Chatzidrosos, G.; Hu, Y.; Zheng, H.; Wickenbrock, A.; Jerschow, A.; Budker, D. Battery Characterization via Eddy-Current Imaging with Nitrogen-Vacancy Centers in Diamond. *Appl. Sci.* **2021**, *11* (7), 3069.
(163) Kubota, K.; Hatano, Y.; Kainuma, Y.; Shin, J.; Nishitani, D.; Shinei, C.; Taniguchi, T.; Teraji, T.; Onoda, S.; Ohshima, T.; Iwasaki, T.; Hatano, M. Wide Temperature Operation of Diamond Quantum Sensor for Electric Vehicle Battery Monitoring. *Diamond Relat. Mater.* **2023**.
(164) Srivastava, S.; Ranjan, S.; Yadav, L.; et al. Advanced spectroscopic techniques for characterizing defects in perovskite solar cells. *Commun. Mater.* **2023**, *4*, 52.
(165) Padilla, M.; Michl, B.; Thaidigsmann, B.; Warta, W.; Schubert, M. C. Short-circuit current density mapping for solar cells. *Sol. Energy Mater. Sol. Cells* **2014**, *120*, 282−288.

https://doi.org/10.1021/acsomega.4c04406
ACS Omega 2025, 10, 2372−2392

(166) Scholten, S. C.; Abrahams, G. J.; Johnson, B. C.; Healey, A. J.; Robertson, I. O.; Simpson, D. A.; Stacey, A.; Onoda, S.; Ohshima, T.; Kho, T. C.; Ibarra Michel, J.; Bullock, J.; Hollenberg, L. C. L.; Tetienne, J.-P. Imaging Current Paths in Silicon Photovoltaic Devices with a Quantum Diamond Microscope. *Phys. Rev. Appl.* **2022**, *18* (1), No. 014041.

(167) Nowodzinski, A.; Chipaux, M.; Toraille, L.; Jacques, V.; Roch, J.-F.; Debuisschert, T. Nitrogen-Vacancy centers in diamond for current imaging at the redistributive layer level of Integrated Circuits. *Microelectronics Reliability* **2015**, *55* (9), 1549−1553. Proceedings of the 26th European Symposium on Reliability of Electron Devices, Failure Physics and Analysis. ISSN: 0026-2714, Elsevier, 2018.

(168) Zhou, B. B.; Jerger, P. C.; Lee, K. H.; Fukami, M.; Mujid, F.; Park, J.; Awschalom, D. D. Spatiotemporal Mapping of a Photocurrent Vortex in Monolayer MoS2 Using Diamond Quantum Sensors. *Phys. Rev. X* **2020**, *10* (1), No. 011003.

https://doi.org/10.1021/acsomega.4c04406
ACS Omega 2025, 10, 2372−2392